

Modeling Redshift Uncertainties in Roman Weak Lensing Cosmology

Diogo H. F. de Souza,^a Boyan Yin,^b Tim Eifler,^c Vivian Miranda,^d Chun-Hao To,^e Brett H. Andrews,^f Katarina Marković,^a Eric Huff,^a Michael A. Troxel,^b Olivier Doré^a

^aJet Propulsion Laboratory, California Institute of Technology, 4800 Oak Grove Drive, Pasadena, CA 91109, USA

^bDepartment of Physics, Duke University Durham, NC 27708, USA

^cDepartment of Astronomy/Steward Observatory, University of Arizona, 933 North Cherry Avenue, Tucson, AZ 85721-0065, USA

^dC.N. Yang Institute for Theoretical Physics, Stony Brook University, NY 11794, USA

^eDepartment of Astronomy and Astrophysics, University of Chicago, Chicago, IL 60637, USA

^fDepartment of Physics and Astronomy, University of Pittsburgh, Pittsburgh, PA 15260, USA

E-mail: souzadio@jpl.nasa.gov

Abstract. Cosmological constraints using weak gravitational lensing measurements from the Roman Space Telescope will require a powerful method for modelling uncertainties in the galaxy redshift distribution. In this work, we use an optimized version of the principal component analysis (PCA) to model uncertainties in the full shape of the redshift distributions, a method proposed by [1] and recently used in the Dark Energy Survey Y6 analysis. Here, we implement this new approach within the Roman High Latitude Imaging Survey (HLIS) Cosmology Project Infrastructure Team (PIT) pipeline, namely Cobaya-Cosmolike Joint Architecture (CoCoA). To validate the PCA in mitigating biases on cosmological parameters, S_8 and Ω_m , we use a set of redshift distributions from **Cardinal** generated for a variety of Roman configurations. Overall, when the simulated cosmic shear data vector is not strongly miscalibrated relative to the fiducial one, both the mean-shift and the PCA-based approaches produce consistent cosmological constraints when marginalizing over nuisance parameters. For mild to strong miscalibration, including additional PCs progressively mitigates biases in S_8 and Ω_m , and can achieve comparable performance with fewer parameters than the nine tomographic-bin mean-shift model.

Contents

1	Introduction	1
2	Simulations of Roman redshift distributions	4
2.1	Synthetic sky mock catalogs	4
2.2	Cardinal simulations	4
2.3	Photometric redshift inference for Roman using SOM	5
2.4	Redshift distribution from wide- and deep-tiers permutations	6
3	Modeling the shape uncertainty of redshift distributions	8
3.1	Constructing the basis functions	8
3.2	Optimizing the basis function with respect to differences in the correlation function	11
4	Analysis methodology	14
5	Results	17
5.1	Baseline results of PCA photo-z mitigation for Roman	18
5.2	Comparison between PCA and mean-shift uncertainty parameterizations	20
5.3	The impact of Roman deep field design on $n(z)$ estimation	21
6	Conclusion	23

1 Introduction

Cosmic shear statistics describe the tiny distortions in the shapes of distant background galaxies. These distortions are caused by the weak gravitational lensing of light as it passes through the intervening matter distribution between us and the ensemble of these source galaxies. Cosmic shear is a powerful and complementary probe of the late universe in the era of precision cosmology [2] when combined with galaxy clustering and galaxy-galaxy lensing, forming the so-called 3×2 pt analysis [3–5]. However constraints on the matter density Ω_m and the amplitude of mass fluctuations σ_8 from the cosmic shear signal are affected by several systematic errors such as intrinsic alignment [6–8], anisotropic point spread function [9], baryonic feedback [10, 11], and uncertainties in the redshift distribution [12], which is the subject of this work. Partitioning the galaxy sample into redshift bins improves the measurement of cosmological parameters [13]. Different redshifts contribute differently to the lensing signal - light from high-z galaxies encounters more structure along the line of sight and thus has a stronger lensing signal. However, [13] points out important caveats that one should consider for optimal extraction of cosmological information from binning the redshift distribution of the galaxies samples, such as the survey depth and the accuracy of the photometric redshift technique. A forecast analysis for next-generation surveys of the impact of imperfect tomographic photometric redshift determination on dynamical dark energy was carried out by [14]. They demonstrated the degeneracies between photometric redshift and dark energy parameters, as well as the resulting degradation in the constraining power on dark energy.

The effects of photo-z uncertainties on tomographic weak lensing cosmology were extensively explored in the Dark Energy Survey (DES) Y1 and Y3 analyses by performing a number of robustness to modeling tests. The redshift distribution for sources galaxies in the weak lensing analysis of the DES Y1 is fully discussed in [15] and [16, 17] for the clustering-based method. Broadly speaking, this procedure consists of obtaining initial estimates of the lensing-weighted redshift distribution by assigning galaxies to four redshift bins using the Bayesian photometric redshift (BPZ) approach of [18], constituting the DES Y1 fiducial analysis. However, several effects contribute to the total uncertainty budget when estimating the redshift distributions, and their impact is commonly compressed into shifts of the mean redshift distribution, $n_i(z) \rightarrow n_i(z - \Delta z_i)$, parameterized by Δz_i , where i denotes the tomographic bin. The constraints of cosmological parameters is performed by marginalizing over the nuisance photo-z parameters, i.e., the Δz_i 's. Beyond the mean-shift parameters, the forecast analysis of [14] also considered a Gaussian scatter to describe the photometric redshift distributions. Although the inclusion of two sets of parameters—the mean shift and the Gaussian scatter—improves the realism of modeling imperfect photometric redshift distributions, in real analyses one must also consider the associated computational cost of introducing additional nuisance parameters. There are several ways to design tests to assess whether photo-z parameters beyond the mean-shift are required to correct imperfections in $n_i(z)$ from the true redshift distribution. The investigation of this question is closely tied to the current survey precision in measuring photometric redshift distributions. For example, the DES-Y1 analysis of cosmological constraints from cosmic shear presented in [19], considered both the BPZ redshift distribution and the resampled high-precision COSMOS2015 [20] which exhibit different shapes in the redshift distribution, particularly in the second tomographic bin (see, e.g., Figure 2 of [19]). At the DES Y1 statistical precision, the difference in the shape of $n_i(z)$ between BPZ and COSMOS is a subdominant contributor to the uncertainties on cosmic shear and does not significantly impact the inference of the cosmological parameters (see, e.g., Figures 9 and 13 of [19] for the 1D and 2D constraints for S_8 and $S_8 - \Omega_m$, respectively). The tomographic weak lensing measurement of [19] for the Λ CDM model reported a 3.5% fractional uncertainty on $\sigma_8(\Omega_m/0.3)^{0.5} = 0.782 \pm 0.027$ at 68% CL (for the DES Y1 3×2 pt analysis see [21]).

From the DES Y3 Gold photometric data set [22], a weak-lensing source galaxy sample was selected [23] and divided into four tomographic bins. The redshift distributions of these bins were calibrated using three independent likelihood-based methods—the Self-Organizing Map $p(z)$ (SOMPZ) [24], clustering redshifts (WZ) [25], and shear ratios (SR) [26]. Together, these complementary techniques yielded consistent and robust constraints on the mean redshift of each bin, achieving an uncertainty of $\sigma_{\langle z \rangle} \approx 0.01$ [27]. The resulting calibrated redshift distributions played a key role in assessing the robustness of the DES Y3 cosmic shear cosmological constraints on both modeling choices and data calibration [28, 29] (see also [30] for the full 3×2 pt analysis). In these studies, the fiducial photometric redshift model parameterizes statistical and systematic calibration uncertainties through the mean redshift shifts, Δz_i . The analysis in [29], however, extended this approach by incorporating the full uncertainty in the shape of the redshift distributions using the Hyperrank formalism [31]. The one- and two-dimensional posterior constraints on S_8 and $S_8 - \Omega_m$ shown in Figures 7 and 10 of [29] demonstrated that the full-shape Hyperrank model yielded results consistent within 1σ of the fiducial DES Y3 analysis.

The Hyperrank approach consists of marginalizing over the range of uncertainty spanned by the ensemble of plausible redshift distributions constructed using the SOMPZ method

from the **Buzzard** simulated photometry catalog for DES Y3. These redshift distributions are ranked according to a descriptive statistic (e.g., the mean redshift) that a priori correlates with the cosmological parameters of interest, such as S_8 . The summary statistic is then used to encode each realization in a optimal relative position of a uniform grid embedded within a unit hypercube. These unit coordinates are sampled in a Markov chain during likelihood inference, and the continuous hyper-parameter value is mapped to a discrete index, which can be decoded to recover the corresponding redshift distribution. However, the performance of Hyperrank depends on balancing the number of redshift realizations, the dimensionality of the hypercube, and the choice of descriptive statistics. Increasing the dimensionality can in principle yield a smoother representation of the posterior, but for a fixed number of realizations this reduces the resolution of the grid and introduces larger spacing between samples. This, in turn, can lead to noisier and less continuous posteriors in the hyper-parameter space, which may hinder sampling efficiency. We refer the reader to [31] for further details on Hyperrank.

An alternative way to marginalize over the shape uncertainty of the redshift distribution is an optimized version of the principal component approach first developed by [1] and used in this work. In this PCA method, a compression matrix \mathbf{E} is constructed to encode the variations in the redshift distributions into a lower-dimensional set of variables \mathbf{u} . This effectively compresses the ensemble into the most informative degrees of freedom, freeing the likelihood of less significant variations in the redshift distribution. A decoder matrix \mathbf{D} is used to build basis functions (we use the terms “PCs” and “modes” interchangeably) to recover an approximation for the redshift distribution represented by the most informative PCs. This technique was used in the DES Y6 analysis for the redshift calibration of sources galaxies [32] and lens galaxies [33]. Overall, this mode-projection method has minimal impact on the cosmological parameters given the statistical power of DES Y6 and the robust constraining power on the full shape of the redshift distributions from SOMPZ and WZ. However, continuing investigation of photo-z uncertainties is needed for next-generation Stage IV surveys, such as the Nancy Grace Roman Space Telescope (Roman) [34–39], the NSF-DOE Vera C. Rubin Observatory Legacy Survey of Space and Time (LSST) [40], and ESA’s Euclid mission [41]. This paper applies the mode-projection technique devised by [1] for redshift distributions simulated for Roman.

This paper is organized as follows: in Section 2 we present a description of simulated redshift distributions for various proposed observing scenarios for the Roman High-Latitude Wide Area Survey (HLWAS) with **Cardinal** simulations. In Section 3, we construct the PCA basis and the optimized mode-projection according to the technique of [1] suitable for the Roman needs. In Section 4 we provide a detailed description of the analysis methodology. In Section 5, we present our main results: (i) a consistency check of our numerical PCA implementation in CoCoA against the prescription proposed by [1]; (ii) an assessment of cosmological parameter constraints obtained with the PCA and mean-shift approaches; and (iii) a more detailed investigation of the various Roman observing scenarios under the PCA method. Finally, in Section 6, we present our summary and conclusion with future perspectives.

2 Simulations of Roman redshift distributions

2.1 Synthetic sky mock catalogs

Investigating biases in different cosmological probes arising from unknown or mismodeled systematic effects is crucial for obtaining unbiased cosmological constraints. To quantify these systematics, it is necessary to generate synthetic sky mock catalogs with a high level of realism. To be useful for systematic control, such catalogs must satisfy several requirements. First, they should cover a volume significantly larger than the targeted survey to ensure that systematic effects remain safely below the level that could bias cosmological inferences. Second, they must include realistic galaxy populations tailored to the specifications of the survey. Third, efficient mock generation is required to enable the incorporation of new techniques and systematic studies [42]. To address these challenges, a wide range of methods for synthetic catalog generation have been developed. In particular, the galaxy-dark matter halo connection framework [43] provides a physically motivated approach; however, mock generation within this framework remains computationally expensive. Phenomenological models offer a practical alternative to mitigate this bottleneck, especially subhalo abundance matching (SHAM) model, a method for mapping galaxy stellar masses or luminosities onto resolved dark matter (sub)halos [44–47], on which the **Buzzard** simulations are based. The **Buzzard** simulations comprise a suite of synthetic sky catalogs that typically include galaxy positions, magnitudes, shapes, photometric errors, and photometric redshift estimates, and was used to support a wide range of DES science analysis [48, 49]. These catalogs are widely used for systematic studies and for testing and validating multiple cosmological probes, such as galaxy clustering and weak lensing analyses. Ultimately, they enable end-to-end validation of the cosmological analysis pipeline, including target selection algorithms such as **redMaGiC** [50] for luminous red galaxies and **redMaPPer** [51] for galaxy clusters. Despite their broad utility, the **Buzzard** simulations exhibit a deficit of **redMaPPer** clusters, with abundances lower by a factor of three to four compared to DES Y1. This mismatch in the simulated galaxy population within cluster environments constitutes a key shortcoming, as realistic cluster galaxy populations are critical for simulation-based evaluations of optically selected cluster detection and characterization [42]. Specifically, one could see discussions that follows Figures 12 and 13 of [48] that shows the deficit in richness at fixed mass when compared to the DES-Y1. As discussed in [52], this issue in the **Buzzard** simulations was likely due to the artificial subhalo disruption, which is then inherited by the **addgals** algorithm via the training process. Attempts to address this issue were made by [44] by including orphan galaxies in SHAM. However, none of the tested models could fit all three stellar mass bins simultaneously, largely because the parameter controlling the asymptotic maximum circular velocity of the halo, strongly affects SHAM predictions. In addition, the models of color-assignment tested in that work underestimates clustering of low-mass red galaxies in the smallest mass bin, which can reduce the number of galaxies in clusters; see [42], [44] and references therein for further details.

2.2 Cardinal simulations

The **Cardinal**¹ simulations [42] solves this deficit of cluster galaxies in **Buzzard** simulations by quantifying and correcting the two main sources of the problem: the artificial subhalo disruption in SHAM and the limitations in the color-assignment scheme. This improved

¹<https://chunhaoto.com/cardinalsim>

model is then passed to the `Addgals` algorithm and generate `Cardinal` catalogs, from LSST bands, constructed from a one-quarter-sky simulation populated with galaxies up to redshift $z = 2.35$ and reaching a limiting magnitude of $m_r = 27$. The galaxy magnitudes, colors and several other galaxy properties are provided through the `Addgals` technique. In the following, we summarize the approach to assign magnitudes and colors to galaxy; firstly, `Cardinal` assumes that galaxy SEDs can be decomposed into five KCORRECT spectral templates [53] with associated coefficients. Therefore, one can map the measured the KCORRECT coefficients from real data and assign then to galaxies in the simulations. From this scheme, one can calculate the observed magnitude by applying band shifts and the observed bandpass without regenerating galaxy SEDs. For the color assignment, the PRIMUS galaxies [54] are used to infer the probability of being red at $z < 0.2$. The `Cardinal` code classifies a galaxy as red if its rest-frame color K-corrected to $z = 0.1$ is above a brightness-dependent threshold of $0.15 - 0.03M_r$, where M_r is the absolute magnitude of a galaxy in the r-band.

2.3 Photometric redshift inference for Roman using SOM

We use the Self Organizing Map Photo-z (SOMPZ) framework with LSST bands [55] to estimate the redshift distribution of the wide tier galaxies for Roman. This method was employed in DES-Y6 for redshift calibration for weak lensing studies, see e.g., Section 4 of [32]. Two SOMs are used inside the framework: The wide tier galaxy are grouped onto the “wide tier SOM” based on their photometry. The deep-field galaxies, which span less area but have additional photometry and depth are grouped onto the “deep SOM”. For each deep-field phenotype (i.e., cell in the two dimensional “deep SOM”). The redshift distribution is obtained using an external redshift calibration sample. In our analysis, we assume it is our deep field sample with perfect spectroscopic redshift information. We then connect the deep-field phenotypes to wide-tier detections under the same observing conditions using `Cardinal` simulation. The wide tier galaxies are further separated into 9 tomographic bins, using an equal-populated approach. In particular, we define our redshift bin edges, and each wide tier SOM cell is assigned to the bin according to the mode of its redshift distribution. These bin edges are iteratively adjusted until each tomographic bin contains an approximately equal number of galaxies.

Each redshift realization represents a possible instance of our redshift distribution under the limitation of our calibration sample. Deep fields, while it greatly improves our redshift calibration by providing additional photometry information to break color-redshift degeneracy, have limited sky area and galaxy therein. Due to the limited sky area, the deep field could not fully represent the fluctuations in the matter density field, with the risk of being in an under- or over-dense region. We measure our sample variance with the same method as [32, 55, 56], which sums the large scale modes in the CAMB-generated [57] matter power spectrum that are not captured within the deep field area.

On the other hand, the finite number of galaxies in the deep field introduce Poisson fluctuation on the number of observed galaxies. The sample variance and shot noise are propagated to our final redshift realizations using a three-step Dirichlet sampling method [32, 55, 56]. In this analysis, we do not include the uncertainty due to the photometry zero-point offsets in our deep field and wide wide tier field, since our goal was to estimate the choice of deep field area and depth on redshift uncertainty. These uncertainty will be included in future analysis.

2.4 Redshift distribution from wide- and deep-tiers permutations

The wide- and deep-tier configurations for the Roman HLWAS scenarios are shown in Table 1. The wide tier is designed to yield about 360 million galaxy shape measurements for weak lensing [58], whereas the deep tier is intended to support the calibration of the cosmological analysis, particularly the uncertainties in shape measurements, photometric redshift estimation, and spectroscopic contamination correction. In principle, biases in the inferred cosmological parameters arising from miscalibrated photometric redshifts could be constrained using the deep fields D1234. However, the simulations used in this work predate the ROTAC Report [58]. For this reason, we do not define a Design Reference Mission (DRM). According to the ROTAC recommendations, the DRM corresponds to a wide-tier configuration closest to W3, with the following updated survey properties: an area of 2415 deg^2 , the same three imaging bands (Y, J, and H), an exposure time of $2 \times 3 \times 107 \text{ s}$, and a depth of 26.4 mag (AB, 5σ point source) in the JH bands.

High Latitude Wide Area Survey					
Tier	Magnitude Error	Exposure Times	Filters	Area	Depth (H)
Wide 1 (W1)	0.20	$5 \times 140 \text{ s}$	YJHF	2000 deg^2	24.96
Wide 2 (W2)	0.25	$5 \times 91 \text{ s}$	H	2000 deg^2	23.93
Wide 3 (W3)	0.25	$5 \times 91 \text{ s}$	YJH	2000 deg^2	24.31
Deep 1 (D1)	0.00	∞	ZYJHFK	20 deg^2	∞
Deep 2 (D2)	0.12	$5 \times 91 \times 4 \text{ s}$	ZYJHFK	20 deg^2	24.93
Deep 3 (D3)	0.12	$5 \times 91 \times 4 \text{ s}$	ZYJHFK	40 deg^2	24.93
Deep 4 (D4)	0.12	$5 \times 91 \times 4 \text{ s}$	ZYJHFK	20 deg^2	25.93

Table 1. The Roman HLWAS proposed scenarios for the wide and deep tiers prior to the ROTAC recommendations of April 24, 2025.

In Table 1, we use the shortened versions of the filter names for compactness, but their full Roman filter names and central wavelengths are as follows: Z (F087), Y (F106), J (F129), H (F158), F (F184), and K (F213). Exposure times (ET) refer to individual exposures of 140 s (or 91 s) using a scan pattern of 5 exposures. The idealized deep field D1 has an infinite exposure time, infinite depth, and zero magnitude error. The deep fields D234 have exposure times $4 \times$ longer than M23. The deep tiers D23 and D4 are 1 and 2 magnitudes deeper than W2, respectively.

- **Wide Tier 1:** This wide tier corresponds to the design reference mission initially proposed in SRD RST-SYS-REQ-0020, Revision D. However, for weak lensing measurements, the ROTAC recommended dropping the F184 photometric band due to its minor impact on photo-z estimation at $z < 3$. Therefore, this makes W3, instead of W1, the closest wide tier scenario to the nominal DRM in the ROTAC report, at least in terms of filters choice. Every Roman HLWAS tier in Table 1 assumes a signal-to-noise ratio (S/R) of 5, then we set a reference for the magnitude error $\sigma_{\text{mag}} \propto 1/\text{S/R} = 0.2$ and scale σ_{mag} for the other tiers according to its exposure time given that $\text{S/R} \propto \sqrt{t_{\text{exp}}}$ where t_{exp} is the exposure time. Finally, W1 has a limiting magnitude in the H band of 24.96 mag (AB, 5σ point source) over 2000 deg^2 .
- **Wide Tier 2:** This wide tier is similar to the in-guide wide tier in terms of filter choice-both use the same single band (H, F158). However, the ROTAC report expands

the wide tier area to 2700 deg^2 , while here we use 2000 deg^2 . The magnitude error increases relative to W1 due to shorter exposure times.

- **Wide Tier 3:** This is the wide tier most similar to the ROTAC recommendation in terms of the three bands (YJH) of the near infrared imaging. W3 has the same σ_{mag} , t_{exp} , and area as W2 but is 0.38 mag deeper.

The deep tiers D1234 in Table 1 incorporate a deep survey component aimed at improving the calibration of cosmological measurements [58] with locations that overlap with the LSST Deep Drilling Fields (DDFs). Every deep field has the same imaging filters ZYJHFK, which adds the Z, F, and K bands compared to W3.

- **Deep Tier 1:** An idealized deep tier with no magnitude error and infinite exposure time, corresponding to an arbitrarily deep limiting magnitude. In principle, such a survey would provide access to a large amount of non-linear information in the power spectrum, since a survey with infinite depth would detect arbitrarily faint objects and high- z galaxies, which are increasingly clustered. It is also the perfect, albeit unrealistic, deep tier for photo-z calibration. Although this tier assumes idealized parameter values for σ_{mag} , t_{exp} , and mag depth, its survey area remains 20 deg^2 and is therefore cosmic-variance limited.
- **Deep Tier 2 & 4:** The deep tiers D2 and D4 are $4\times$ longer than W2 over 20 deg^2 , being +1 and +2 deeper than W2, respectively.
- **Deep Tier 3:** This tier enables relatively easier cosmological constraints and photo-z calibration, as it has a shallower depth (1 mag shallower than D4) and covers a wider area (20 deg^2 larger than D124). The increased area helps reduce cosmic variance in the power spectrum by including more information from linear scales, while the shallower depth excludes the faintest objects detected in D4. This deep tier is better constrained than the D124 deep tiers.

By updating the subhalo abundance matching framework and introducing a new color assignment scheme (see Appendix K of [42] for a summary of the improvements from `Buzzard` 2.0 to `Cardinal`), the `Cardinal` mock catalogs enable a wide range of applications. These include (i) studies of optically selected galaxy clusters to quantify selection biases, (ii) evaluation of small-scale lensing systematics using the latest ray-tracing implementation in `Calclens` [59], (iii) end-to-end tests of multi-probe cosmological analysis, and (iv) investigations of photometric redshift performance (see [42] for further details on each of these points). In this work, we focus on the latter application. Specifically, the `Cardinal` code enables us to study how redshift errors in deep-field surveys affect photometric redshift calibration, and how sample variance due to the limited area of deep fields propagates into redshift uncertainties for wide-field galaxies. By permuting different configurations of the deep and wide tiers, we form the scenarios shown in Figure 1, where we generate ensembles of redshift distributions and then, in the next sections, we show how we evaluate their impact on cosmological parameter constraints, such as Ω_m and S_8 . In Figure 1 we notice, however, a minor caveat; the `Cardinal` simulations were not designed to span all wide-deep field permutations, and the D3 configuration was included solely as a targeted stress test of a larger deep field for the baseline wide-field scenarios (M1 and M2), which is why no Scenario M3-D3 combination was generated. A subsample of 100 realizations are shown as fainter lines in Figure 1 with

the scatter reflecting the uncertainty in their estimation. The mean of the full ensemble is represented by the darker, dashed line, whereas different colors and panels represent different Roman scenarios, as indicated by the inner legend.

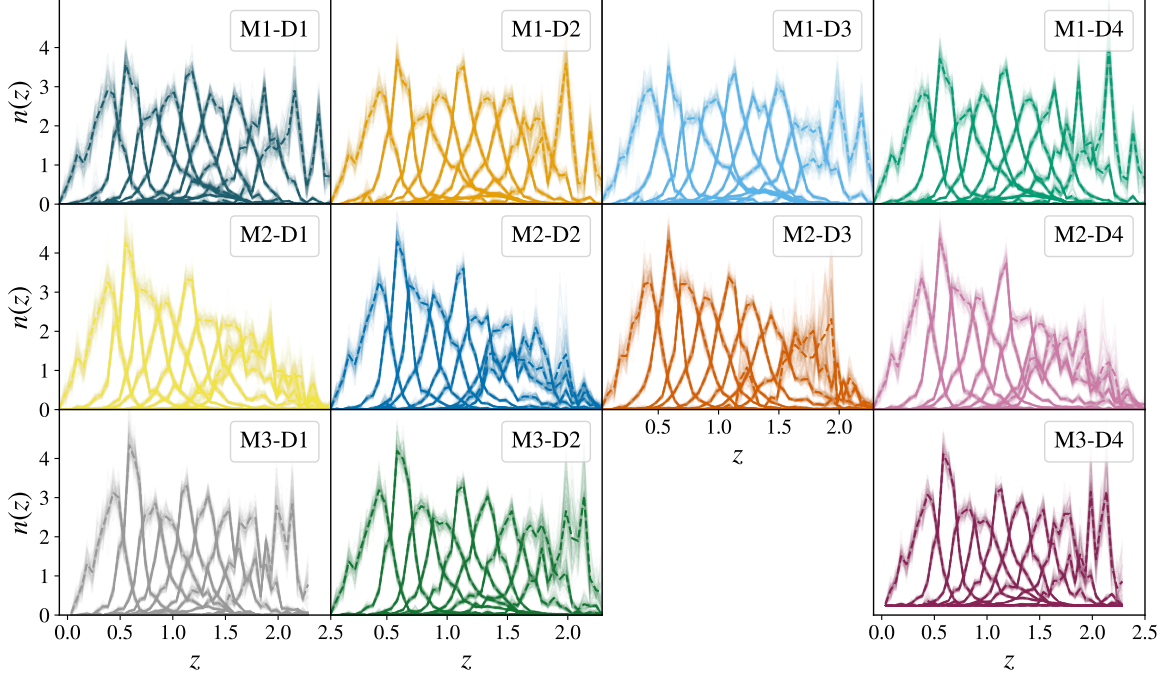


Figure 1. Estimated redshift distributions for different wide- and deep-tier specifications. Lighter lines display a small illustrative subsample of 100 (out of 1 million) realizations, with their spread reflecting the uncertainty in their exact shape, whereas the darker dashed lines show the mean redshift distribution computed over all 1 million realizations. Each row pairs a fixed wide tier (W1-W3) with a deep tier (D1-D4), except for the combination W3-D3.

3 Modeling the shape uncertainty of redshift distributions

3.1 Constructing the basis functions

Let \mathbf{n}_r denote a single realization from the ensemble of $N_{\text{sim}} = 1,000,000$ redshift distributions generated with `Cardinal` (see Figure 1). Each realization is defined over $N_t = 9$ tomographic bins (indexed by b) and $N_z = 46$ redshift points (indexed by k) per tomographic bin. To represent \mathbf{n}_r as a single vector, we stack the values from all tomographic bins, yielding a vector of length $N_{\text{data}} \equiv N_t N_z = 414$. Stacking all N_{sim} realizations column-wise produces the matrix \mathbf{n} of dimension $N_{\text{data}} \times N_{\text{sim}}$. Thus, each column of \mathbf{n} corresponds to one realization \mathbf{n}_r , and each element n_{rbk} is uniquely specified by the realization index r , tomographic-bin index b , and redshift index k :

$$\mathbf{n}_r \equiv \{n_{rbk} | r \in 1, \dots, N_{\text{sim}} | b \in 1, \dots, N_t | k \in 1, \dots, N_z\}. \quad (3.1)$$

For a fixed tomographic bin index b and redshift point k , we have 1 million values of n_{rbk} , whose variance reflects the uncertainty in their determination. We apply the principal

component method to linearly transform the data points n_{rbk} into a new coordinate system, such that the directions (principal components, or modes) correspond to the axes of maximal variance in the data.

The first step is to center the data around the mean redshift distribution $\bar{\mathbf{n}}$ by computing the difference matrix Δ , defined as the difference between each realization and the mean

$$\bar{\mathbf{n}} \equiv \langle \mathbf{n} \rangle_{\text{sim}} = \frac{1}{N_{\text{sim}}} \sum_{r=1}^{N_{\text{sim}}} \mathbf{n}_r,$$

$$\Delta \equiv \mathbf{n} - \bar{\mathbf{n}} = [\mathbf{n}_{r=1} - \bar{\mathbf{n}} \mid \mathbf{n}_2 - \bar{\mathbf{n}} \mid \cdots \mid \mathbf{n}_{N_{\text{sim}}} - \bar{\mathbf{n}}]_{N_{\text{data}} \times N_{\text{sim}}}. \quad (3.2)$$

The length of $\bar{\mathbf{n}}$ is N_{data} , while Δ has the same dimensions as \mathbf{n} , namely $N_{\text{data}} \times N_{\text{sim}}$. Figure 2 is an example of these two quantities for the Roman scenario W1-D1. The top panel is the mean redshift distribution (the same mean as shown in Figure 1), and the bottom panel are the first 100 columns of the difference matrix arranged by the N_t tomographic bins.

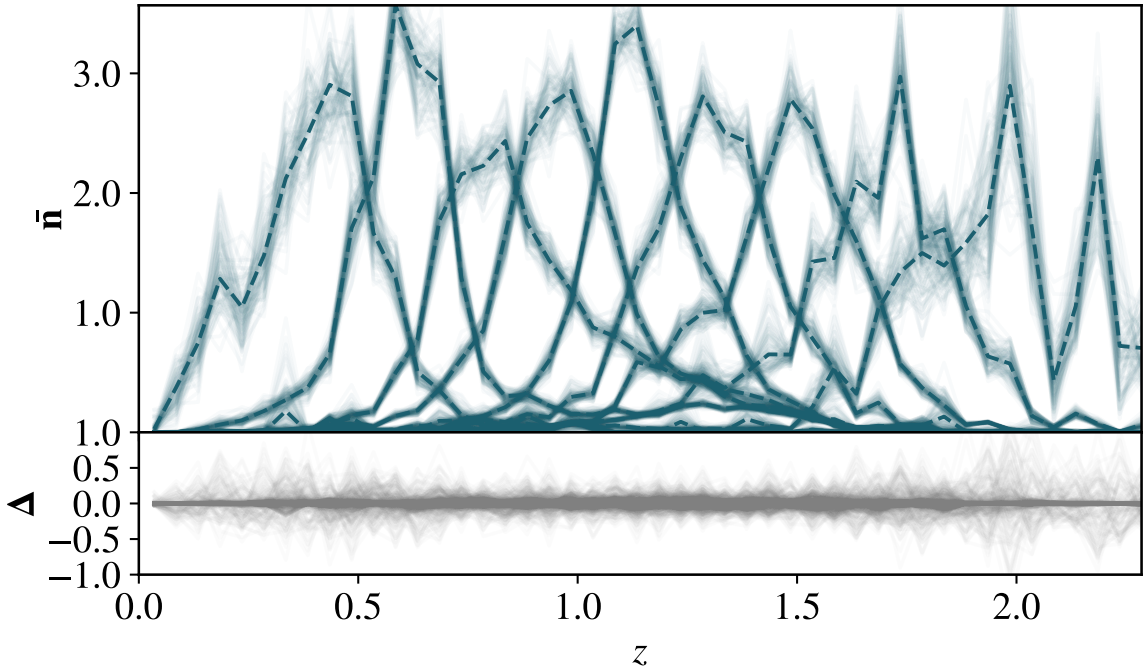


Figure 2. Quantities derived from the Roman scenario W1-D1. *Top:* mean redshift distribution (dark dashed lines) obtained from the ensemble of 1 million realizations, along with 100 individual realizations (faint lines). *Bottom:* difference between the mean redshift distribution and the individual realizations per tomographic bin.

The principal components are computed from the singular value decomposition (SVD) of the difference matrix

$$\Delta = \mathbf{D} \Sigma \tilde{\mathbf{U}}^T. \quad (3.3)$$

The factorization in Equation (3.3) is illustrated in Figure 3 (cf. Figure 5 of the baryon PCA used by [11]). In this decomposition, the *decoding* matrix \mathbf{D} and the matrix $\tilde{\mathbf{U}}^T$ are unitary

Figure 3. Singular value decomposition of the difference matrix Δ for the $N_{\text{sim}} = 10^6$ realizations for the redshift distributions. The unitary matrix \mathbf{D} holds the left singular vectors and $\tilde{\mathbf{U}}^T$ contains the right singular vectors, while Σ possesses the singular values; the upper 414×414 block contains the positive real singular values $\sigma_1, \dots, \sigma_{414}$ in decreasing order, and the dashed square indicates that all remaining entries are zero.

and have dimensions $N_{\text{data}} \times N_{\text{data}} = 414 \times 414$ and $N_{\text{sim}} \times N_{\text{sim}} = 10^6 \times 10^6$, respectively. The matrix Σ has dimensions $N_{\text{data}} \times N_{\text{sim}} = 414 \times 10^6$, whose upper 414×414 block contains the positive real singular values $\sigma_1, \sigma_2, \dots, \sigma_{414}$ in decreasing order, and the remaining entries are zero, as indicated by the dashed square. The columns of \mathbf{D} correspond to the PCs (or eigenvectors) of the covariance matrix

$$\mathbf{C}_\Delta \equiv \Delta \Delta^T, \quad (3.4)$$

with the eigenvalues given by the diagonal elements of $\Sigma \Sigma^T$. Interestingly, the SVD of Δ is equivalent to the eigendecomposition of “ C_n ” used in [1]. To keep the notation used here as close as possible to [1], we denote PCs modes by \mathbf{U}_i . To represent any redshift distribution in the basis of the principal components, we use the first $M (\leq N_{\text{data}})$ columns \mathbf{U}_i of the matrix \mathbf{D}

$$\hat{\mathbf{n}} = \bar{\mathbf{n}} + \sum_{i=1}^M u_i \mathbf{U}_i, \quad (3.5)$$

where u_i are the amplitudes (or projection coefficients) of the PCs. In Figure 3 the i th PC in the b th tomographic bin is denoted by $\mathbf{U}_i^b(z)$ where the indexes range are $i = 1, \dots, N_{\text{data}}$ and $b = 1, \dots, N_t$. In Figure 4, we present a two-dimensional example of the PCA method applied to the ensemble of realizations derived from Equation (3.1):

The PCA approach presented so far constructs basis functions directly from the SVD of the ensemble of realizations around the mean redshift distribution. However, it does not account for how each realization impacts the cosmic shear power spectra. Consequently, the inferred cosmological parameters are only weakly sensitive to the redshift-distribution uncertainty captured by these unweighted principal components. An optimized, signal-aware PCA incorporating weights that encode the response of shear observables to fluctuations in \mathbf{n} is introduced in the next section, following [1].

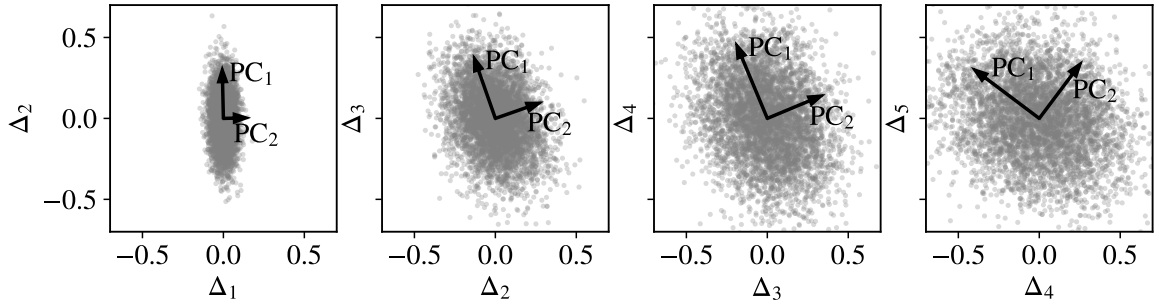


Figure 4. Two-dimensional projection of the ensemble of the SVD application to the redshift distributions of Roman scenario W1-D1. Gray points represent draws from a Gaussian distribution with mean zero and a covariance matrix. The correlations between dimensions are captured by the covariance of the difference vectors Δ_i . The arrows indicate the first (\mathbf{PC}_1) and second (\mathbf{PC}_2) principal components.

3.2 Optimizing the basis function with respect to differences in the correlation function

To propagate the variance of the ensemble of redshift distributions to the cosmic shear power spectra and the cosmological parameters in the Markov chain, we need to compute the Fisher matrix \mathbf{F} (cf [1] for details):

$$\mathbf{F} \equiv \left[\frac{\partial \xi_{\pm}}{\partial \mathbf{n}} \right]_{\bar{\mathbf{n}}}^T \mathbf{C}_{\xi_{\pm}}^{-1} \left[\frac{\partial \xi_{\pm}}{\partial \mathbf{n}} \right]_{\bar{\mathbf{n}}}, \quad (3.6)$$

where the Jacobian matrix \mathbf{J} is:

$$\mathbf{J} \equiv \frac{\partial \xi_{\pm}}{\partial \mathbf{n}}. \quad (3.7)$$

To compute $\xi_{\pm}(\theta)$ and the Jacobian matrix, we use the Cobaya-Cosmolike Joint Architecture, CoCoA². The correlation function is evaluated in 15 angular bins between $\theta_{\min} = 2.5$ arcmin, and $\theta_{\max} = 250$ arcmin. The derivative in Equation (3.7) is evaluated with the five-point stencil forward finite difference method:

$$f'(x) \approx \frac{1}{12\epsilon} \left[-25f(x) + 48f(x + \epsilon) - 36f(x + 2\epsilon) + 16f(x + 3\epsilon) - 3f(x + 4\epsilon) \right],$$

where $f \rightarrow \xi_{\pm}(\theta; x)$ and $x \rightarrow n_{rbk} = \mathbf{n}_r(z_k)$ at the b th tomographic bin. The one-sided forward derivative is chosen to prevent negative shifts in x , since it represents redshift distributions. To compute the covariance matrix of Equation (3.6) we

We employ *CosmoCov*³ [60, 61] to evaluate the Gaussian covariance matrix for the 3×2 point-correlation function. The CoCoA framework is then used to derive the masked covariance matrix for the cosmic shear component, $\mathbf{C}_{\xi_{\pm}}$. Finally, we combine \mathbf{J} with the inverse of $\mathbf{C}_{\xi_{\pm}}$, following Equation (3.6), to construct the Fisher matrix. The Fisher matrix and the sample covariance, $\mathbf{C}_{\Delta} = \Delta \Delta^T$, form the starting point of the dimensionality-reduction

²<https://github.com/CosmoLike/cocoa>

³<https://github.com/CosmoLike/CosmoCov>

procedure. Together, they are used to identify the optimal basis functions. The subsequent steps involve constructing the encoding matrix \mathbf{E} , which projects the centered realizations (i.e., the difference matrix) onto the principal-component basis, and the decoding matrix \mathbf{D} , which reconstructs the redshift distribution using only the M most significant modes. The value of M is determined by a threshold criterion on the loss of cosmological information, quantified by $\langle \chi^2 \rangle$ between the fiducial summary statistics (in our case, ξ_{\pm}) and the theoretical statistics computed from the compressed redshift distributions. We refer the reader to [1] for further details on derivation of these matrices, and [32, 33] for application of these method in DES Y6.

Figure 5 presents the first four principal components (PC_1, \dots, PC_4) and the last four ($PC_{411}, \dots, PC_{414}$) derived from the Roman W1-D1 scenario, separated according to their contributions across the nine tomographic bins. The reader can qualitatively compare these Roman components with those obtained for DES, shown in Figure E2 of [32]. In Figure 6 we show the complete set of principal components corresponds to the columns of the decoding matrix \mathbf{D} . The PCs oscillate near the center of each tomographic bin, as indicated by the darker red and blue regions in the heat map, while their contributions becomes negligible in the transition regions between bins, visible as blank gaps. Since the decoding matrix is ordered from the most to the least significant components, those beyond $M > 300$ in Figure 6 are essentially negligible for a given tomographic bin, as indicated by the amplitudes of order $\mathcal{O}(10^{-11})$ in the last four rows of Figure 5. The impact of each principal component on the redshift distribution should be evaluated using its individual amplitude u_i , since, according to Equation (3.5), the contribution scales with the product $u_i \mathbf{U}_i$.

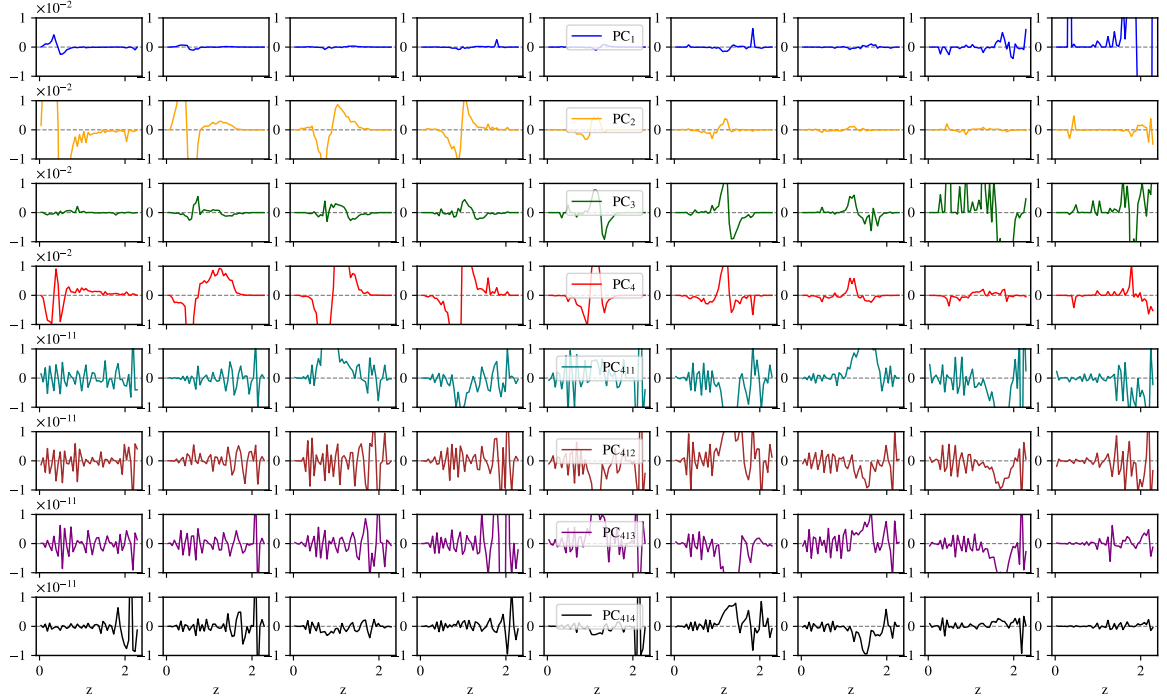


Figure 5. The first four and the last four PC modes, as function of the redshift, across the nine tomographic redshift bins for the Roman scenario W1-D1.

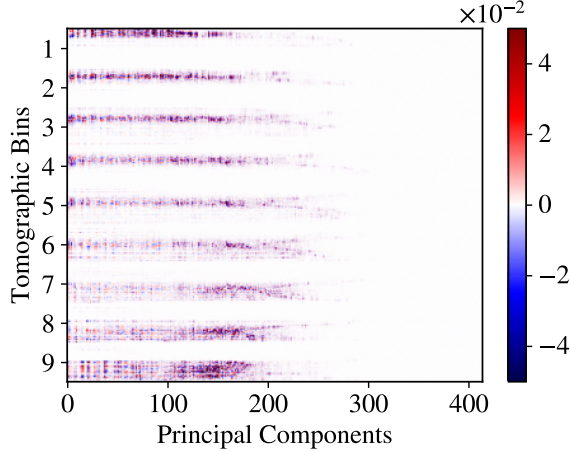


Figure 6. Decoding matrix, or the principal components \mathbf{D}

The distribution of the projected amplitudes u_i s for the ensemble of 1 million redshift distribution can be obtained by applying the encoding matrix (see [1])

$$\mathbf{u} = \mathbf{E}\Delta, \quad (3.8)$$

or by projecting the difference matrix $\hat{\Delta} = \hat{\mathbf{n}} - \bar{\mathbf{n}}$ onto the PCs as per Equation (3.5) and summing over every redshift point and tomographic bin

$$u_i = \langle \hat{\Delta}, \mathbf{U}_i \rangle = \sum_{b=1}^{N_t} \sum_{k=1}^{N_z} \hat{\Delta}_{bk} \cdot \mathbf{U}_{bki}. \quad (3.9)$$

The prior probability distributions of the first five projected amplitudes, u_i , for the Roman scenario W1-D1 are shown in the upper-triangle plot of Figure 7 (dark green region). The label “E: 1, Δ : 1” indicates that both the encoding matrix \mathbf{E} and the ensemble of centered realizations Δ are derived from the same Roman scenario W1-D1 (see Equation (3.8)). As expected, the amplitudes are uncorrelated and centered around zero, making the u_i well approximated by a Gaussian distribution with mean zero and unit variance, represented by the dotted black lines in Figure 7. In Section 5, we use this prior information in our MCMC analysis. In principle, however, \mathbf{E} and Δ can be drawn from different Roman scenarios, shown in the lower triangle plot of Figure 7. For instance, the configuration “E: 2, Δ : 1” corresponds to principal components derived from a noisier Roman scenario W2-D2 applied to a synthetic cosmic shear data vector based on the idealized W1-D1 scenario (see Table 1), and vice versa for “E: 1, Δ : 2”. Mixing the Roman scenarios slightly reduces the Gaussianity of the amplitude distributions, a case we examine in more detail in Section 5.

Having established all the necessary components, we are now equipped to perform a likelihood analysis using the new PCA framework. The main steps of the (un)weighted PCA pipeline are summarized and illustrated in Figure 8: (i) Using **Cardinal**, we generate one million realizations of the redshift distributions. (ii) Compute the covariance matrix \mathbf{C}_Δ of the samples, centered around the mean distribution $\bar{\mathbf{n}}$. The square matrix \mathbf{C}_Δ is then decomposed into its eigenvectors \mathbf{V} and eigenvalues Λ . Stopping here yields the unweighted PCA method, where the PCs are given by \mathbf{V} (or equivalently, by the \mathbf{D} matrix derived from

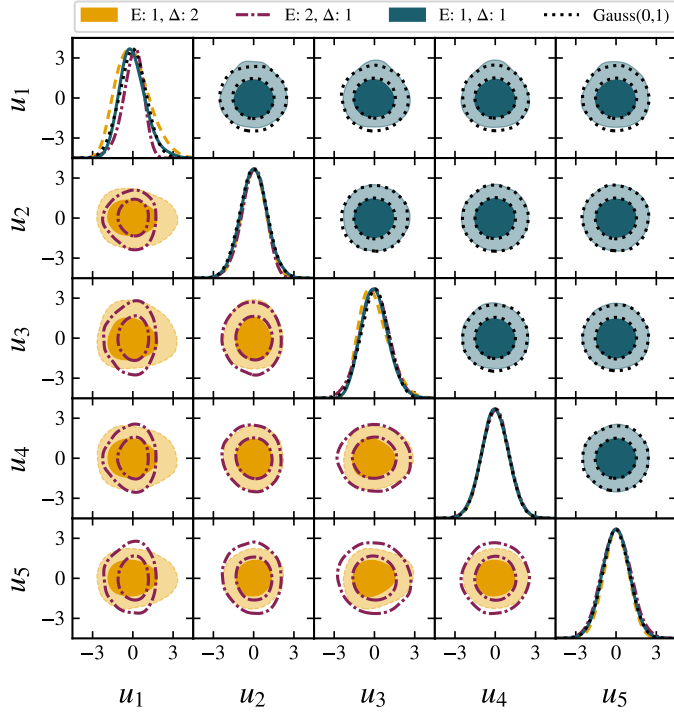


Figure 7. Prior probability distributions of the first five projected amplitudes, u_i , along with Gaussian fits shown as dotted black lines. *Upper triangle*: both the encoding matrix and the difference matrix are derived from the same Roman scenario, W1-D1. *Lower triangle*: the yellow shaded region indicates that the encoding matrix is derived from W1-D1 and the difference matrix from W2-D2, while the purple dash-dotted line represents the reverse case, where the encoding matrix is derived from W2-D2 and the difference matrix from W1-D1.

the SVD of Δ). (iii) With `CosmoCov` and `CoCoA`, compute the covariance of the observable ξ_{\pm} and the Jacobian matrix $\mathbf{J} = \partial \xi_{\pm} / \partial \mathbf{n}$. (iv) Combine \mathbf{J} with the inverse of $\mathbf{C}_{\xi_{\pm}}$ to obtain the Fisher matrix \mathbf{F} . (v) Derive the transformed Fisher matrix \mathbf{G} (see [1]), from which we construct the “encoding” matrix \mathbf{E} and the “decoding” matrix \mathbf{D} . (vi) The columns of \mathbf{D} represent the principal components (modes) that define the PCA model for the redshift distribution. (vii) In the MCMC analysis, we sample over the PC amplitudes u_i to assess their impact on cosmological parameter constraints (e.g., σ_8 versus Ω_m). The pipeline shown in Figure 8 is implemented in `CoCoA` and available at `cocoa_photoz`⁴.

4 Analysis methodology

The posterior distributions of the cosmological parameters are inferred through a Markov Chain Monte Carlo (MCMC) approach, with convergence evaluated using the Gelman-Rubin statistic, requiring $R - 1 < 0.015$. The Bayesian analysis is performed with `Cobaya`⁵ [62], while theoretical predictions are computed using `CAMB`⁶ [63] and `CosmoLike` within the `CoCoA`

⁴https://github.com/Roman-HLIS-Cosmology-PIT/cocoa_photoz

⁵<https://github.com/CobayaSampler/cobaya>

⁶<https://github.com/cmbant/camb>

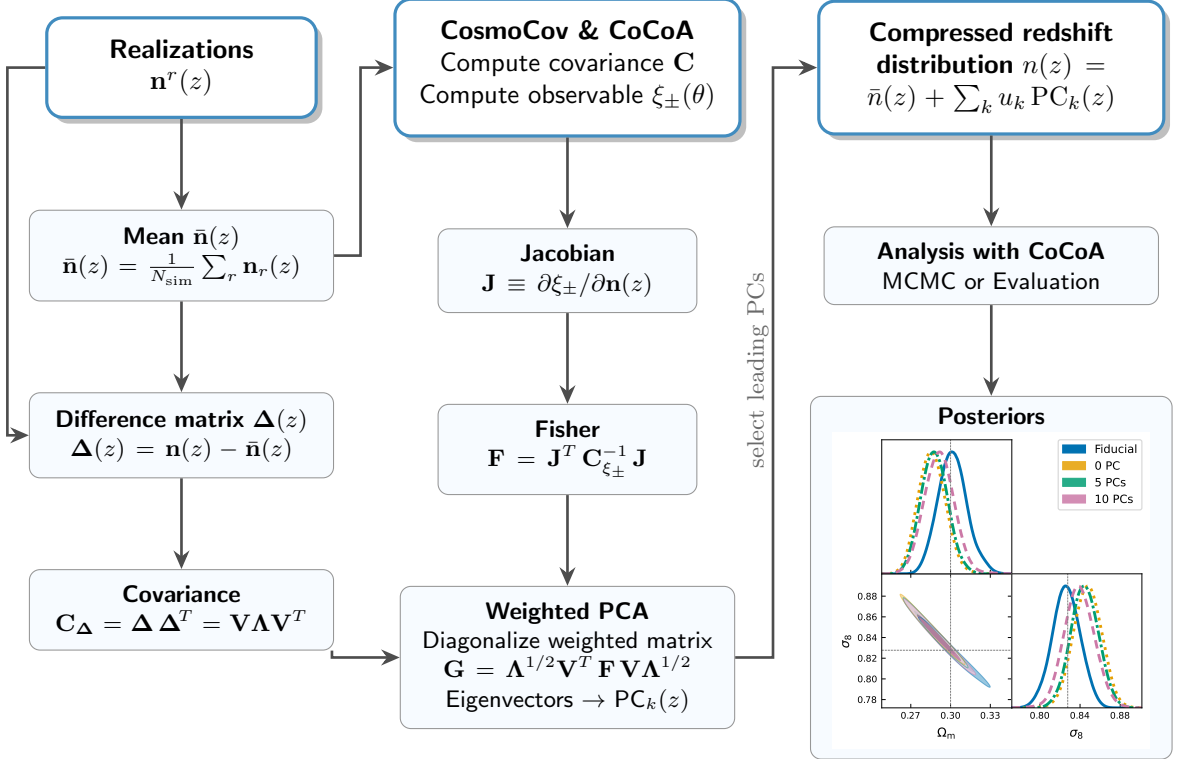


Figure 8. Pipeline workflow for the $n(z)$ PCA method implemented in CoCoA.

framework. The resulting MCMC chains are analyzed and visualized with `GetDist`⁷ [64].

The synthetic cosmic shear power spectra is generated given a redshift distribution (e.g., any normalized $n(z)$ shown in Figure 1), and the fiducial cosmological parameters listed in Table 2. The parameters varied in the MCMC chains are the total matter density Ω_m , baryon density Ω_b , Hubble constant H_0 , amplitude of primordial fluctuations A_s , and scalar spectral index n_s . The optical depth τ is held fixed, and the neutrino sector is set to the default `CAMB` configuration-one massive neutrino with $m_\nu = 0.06$ eV, degenerate mass eigenstates, and an effective number of neutrinos $N_{\text{eff}} = 3.044$. For the Λ CDM model, the Chevallier-Polarski-Linder (CPL) parameters are fixed to $w_0 = -1$ and $w_a = 0$. The Survey parameters are the total sky are, Ω_s , the total shape noise of weak lensing measurements, σ_ϵ , and the number density in each bin, n_g . In this work, we consider two models according to Table 2: (i) Λ CDM+Shift - the standard analysis in which the amplitudes of the principal components are fixed to zero while the mean-shift parameters are varied; and (ii) Λ CDM+PCA - the case where the mean-shift parameters are fixed in the chain and the amplitudes of the principal components are varied. Note that the index i associated with Δ_z^i refers to the tomographic bins, whereas when associated with u_i , it denotes the i th principal component amplitude. Each PC \mathbf{U}_i has a single amplitude u_i shared across all nine tomographic bins; however, the product $u_i \mathbf{U}_i$, as defined in Equation (3.5), differs between bins because the intrinsic shape of \mathbf{U}_i varies with tomographic bin.

We use as the synthetic data vector the two tomographic cosmic shear correlation func-

⁷<https://github.com/cmbant/getdist>

Parameter	Fiducial	Prior
Cosmology		
Ω_m	0.3	flat (0.1, 0.6)
Ω_b	0.04	flat (0.04, 0.055)
H_0	67.32	flat (60, 76)
$10^9 A_s$	2.1	flat (1.1, 2.8)
n_s	0.966	flat (0.87, 1.07)
$\sum m_\nu$	0.06	fixed
τ	0.0697	fixed
w_0	-1	fixed
w_a	0	fixed
Survey		
Ω_s	2000 deg ²	fixed
σ_ϵ	0.39	fixed
n_g	40 gal/arcmin ²	fixed
Shear calibration		
$m_i, i \in [1, 9]$	0	Gauss (0.0, 0.005)
Source photo-z		
$\Delta_z^i, i \in [1, 9]$	0	Gauss (a): (0, 0.003)
$\Delta_z^i, i \in [1, 9]$	0	Gauss (b): (0, 0.01)
PCA		
$\Delta_z^i, i \in [1, 9]$	0	fixed
$u_i, i \in [1, M]$	0	Gauss (0, 1)

Table 2. Fiducial values and priors for cosmological, survey, and systematic parameters. The Cosmology, Survey, and Shear Calibration blocks define the baseline Λ CDM model, the properties of our adopted fiducial Roman survey, and the shear calibration nuisance parameters, respectively. The Source photo-z and PCA blocks represent a modification of this baseline; when the former are varied in a MCMC, the latter are fixed to the fiducial values, and vice-versa.

tions $\xi_\pm^{ij}(\theta)$, where the \pm denotes the sum and difference of the tangential- and cross-components of the projected galaxy shape distortion due to weak gravitational lensing. We compute the cosmic shear in 15 angular bins, uniformly spaced in logarithmic scale covering the range $\theta_{\min} = 2.5$ arcmin to $\theta_{\max} = 250$ arcmin.

The shear signal is a combination of the gravitational shear (hereafter κ) and intrinsic alignments, and these are decomposed into the leading- and higher-order weak lensing effects denoted by the E- and B-mode components, respectively. The connection between the correlation function in Real space with the power spectra in Fourier space is as follows [29, 30]:

$$\xi_\pm^{ij}(\theta) = \sum \frac{2\ell + 1}{2\pi\ell^2(\ell + 1)^2} \left[G_{\ell,2}^+(\cos\theta) \pm G_{\ell,2}^-(\cos\theta) \right] \left[C_{EE}^{ij}(\ell) \pm C_{I_B I_B}^{ij}(\ell) \right], \quad (4.1)$$

where the two auxiliary functions $G_{\ell,m=2}^\pm(x)$ are obtained from the Legendre polynomials

[65, 66]. Each E/B-mode term is given by [66]:

$$C_{EE}^{ij}(\ell) = C_{\kappa\kappa}^{ij}(\ell) + C_{\kappa I_E}^{ij}(\ell) + C_{\kappa I_E}^{ji}(\ell) + C_{I_E I_E}^{ij}(\ell), \quad (4.2)$$

$$C_{BB}^{ij}(\ell) = C_{I_B I_B}^{ij}(\ell). \quad (4.3)$$

The gravitational shear, represented by the first term in Equation (4.2), can be expressed in the Limber approximation as in [67–69]:

$$C_{\kappa\kappa}^{ij}(\ell) = \int_0^{\chi_h} d\chi \frac{W_\kappa^i(\chi) W_\kappa^j(\chi)}{\chi^2} P_{\text{NL}}\left(\frac{\ell + 1/2}{\chi}, z(\chi)\right), \quad (4.4)$$

where χ is the comoving radial distance, $z(\chi)$ is the redshift at comoving distance χ , and χ_h is the comoving horizon distance. The 3D nonlinear matter power spectrum, P_{NL} , is computed using the Takahashi halofit fitting formula [70], and for the intrinsic alignment we consider the Non-Linear Alignment (NLA) model [71–73].

The lens efficiency kernel in the i -th tomographic bin in Equation (4.4) is given by [69]:

$$W_\kappa^i(\chi) = \frac{3H_0^2\Omega_m\chi}{2a(\chi)} \int_\chi^{\chi_h} d\chi' \left(\frac{\chi' - \chi}{\chi}\right) n_\kappa^i(z(\chi')) \frac{dz}{d\chi'}, \quad (4.5)$$

where H_0 is the Hubble constant, Ω_m is the matter density, and $a(\chi)$ is the scale factor at comoving distance χ . The source galaxy redshift distribution in tomographic bin i is denoted by $n_\kappa^i(z)$ with uncertainties in its shape parameterized through the mean-shift Δ_z^i or the amplitude of the PCs u_i 's.

Starting from a chosen redshift distribution $n(z)$ shown in Figure 1, together with the fiducial cosmology listed in Table 2 and an assumed covariance matrix, we compute the posterior distribution $P(\boldsymbol{\theta}|\mathbf{D})$ using Bayes' theorem $P(\boldsymbol{\theta}|\mathbf{D}) \propto \mathcal{L}(\mathbf{D}|\boldsymbol{\theta})P(\boldsymbol{\theta})$ where $P(\boldsymbol{\theta})$ is the prior and $\mathcal{L}(\mathbf{D}|\boldsymbol{\theta})$ is the likelihood function, given by

$$L(\mathbf{D}|\boldsymbol{\theta}, \hat{\mathbf{n}}) \propto \exp\left[-\frac{1}{2}(\mathbf{D} - \mathbf{M})^T \mathbf{C}^{-1} (\mathbf{D} - \mathbf{M})\right]. \quad (4.6)$$

The synthetic cosmic shear data vector is denoted by \mathbf{D} , and the model prediction by $\mathbf{M}(\boldsymbol{\theta}, \hat{\mathbf{n}})$. The parameter vector is decomposed as $\boldsymbol{\theta} \rightarrow \boldsymbol{\theta}, \hat{\mathbf{n}}$ to distinguish the cosmological parameters $\boldsymbol{\theta}$ from those describing the redshift-distribution model-either the mean-shift or the compressed redshift distribution. Reference [1] presents a linearized approximation to the χ^2 derived from Equation (4.6). In the next section, we compare this linearized approach with the full χ^2 evaluation.

5 Results

In this section, we present the results of our PCA-based parameterization of uncertainties in the redshift-distribution shapes and compare them with the standard mean-shift approach. For both PCA and mean shift, we first select one Roman scenario from Figure 1 to define the fiducial redshift distribution and adopt the fiducial cosmological parameters in Table 2 to construct the synthetic cosmic shear data vector. The choice of a specific realization $\mathbf{n}^r(z)$ among the one million available is determined by the chi-squared value $\chi_{\text{ini},r}^2$ computed at those fiducial parameters. The mean-shift method requires only this setup, after which nine

nuisance parameters Δ_z^i are varied in the MCMC runs. The PCA-based method introduces two additional steps: selecting a Roman scenario to train the PC modes (\mathbf{U}_i) and choosing how many PC amplitudes (u_i) to vary in the MCMC analyses. As a result, the PCA workflow involves two independent scenario choices—one for defining the fiducial simulated cosmic shear data vector and another for generating the PC basis. When these coincide, we refer to the case as “non-mixing”; when they differ, we refer to it as “mixing”.

To evaluate how effectively the PCA and mean-shift methods mitigate biases, we follow the definitions in [11], with a slight adjustment to the error estimate: the bias is defined as the difference between the fiducial value and the best-fit, and the error is taken as half of the 2σ width of the 1D marginalized constraint on the parameter of interest. In addition, we present the resulting 2D marginalized posterior distributions for Ω_m and S_8 .

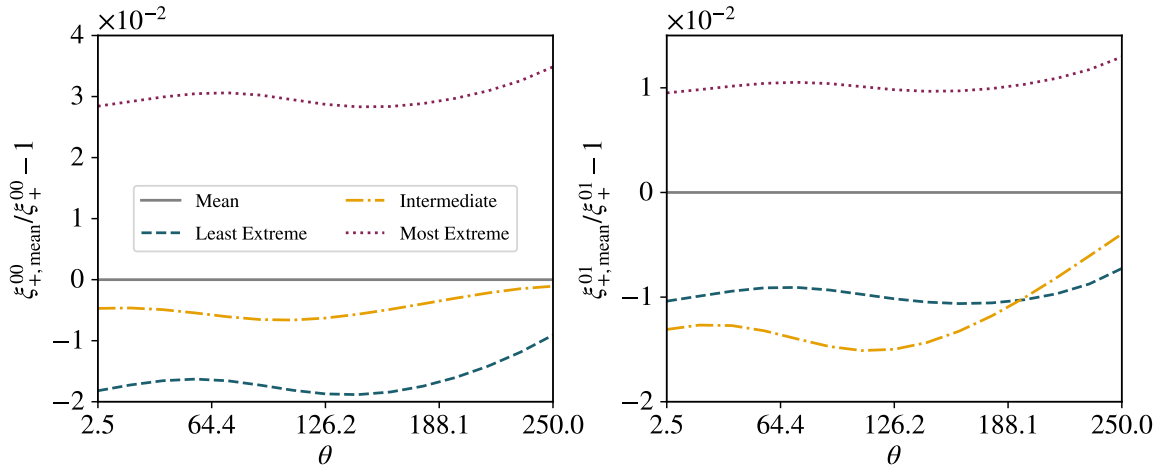


Figure 9. The relative difference of the cosmic shear two-point function $\xi_+^{ij}(\theta)$ for the auto-correlation, $i = 0, j = 0$, and the cross-correlation, $i = 0, j = 1$, as function of the angular binning, θ , in three different cases of the redshift distribution: “least extreme” (green dashed line), “intermediate” (orange dashed dotted), and “most extreme” (dotted purple). The gray line at 0 corresponds to the mean redshift distribution. The least extreme realization has $\chi_{\text{ini},\text{least}}^2 = 5$, the intermediate realization has $\chi_{\text{ini},\text{inter}}^2 = 35$, and the most extreme realization has $\chi_{\text{ini},\text{most}}^2 = 1004$.

5.1 Baseline results of PCA photo-z mitigation for Roman

We start with the “non-mixing” choice of Roman scenarios, adopting the same W1-D1 to build both the synthetic cosmic shear data vector and the PCs. We then compute a single likelihood evaluation for several realizations r to obtain the initial chi-squared values, $\chi_{\text{ini},r}^2$. Each evaluation with `CoCoA` takes about 0.18 seconds, allowing us to quickly estimate the goodness of fit. The realization indices r are then ranked in order of increasing $\chi_{\text{ini},r}^2$, and three representative cases are selected: the “least extreme” realization, defined by $\chi_{\text{ini},\text{least}}^2$, with an arbitrarily low value; the “most extreme” realization, $\chi_{\text{ini},\text{most}}^2$, with an arbitrarily high value; and the “intermediate” realization, $\chi_{\text{ini},\text{inter}}^2$, with a value between the previous two. The impact of this illustrative, arbitrary selection on $\xi_+^{ij}(\theta)$ and on χ^2 as a function of the number of PCs is shown in Figures 9 and 10, respectively. The results correspond to the least, intermediate, and most extreme $\mathbf{n}(z)$ realizations, with initial reduced chi-square

values $\chi_{\text{ini},r}^2 = 5, 35$, and 1004 , respectively. In Figure 9, we show, for tomographic bins combinations $i = 0, j = 0$ and $i = 0, j = 1$, how each of these three cases of $\chi_{\text{ini},r}^2$ affects the correlation function $\xi_{\pm}^{ij}(\theta; \mathbf{n}_r)$ relative to $\xi_{\pm}^{ij}(\theta; \bar{\mathbf{n}})$ computed using the mean redshift distribution $\bar{\mathbf{n}}$. Albeit the least and intermediate cases can alternate their absolute values, we see that the most extreme realization possess the largest deviation relative to $\xi_{\pm}^{ij}(\theta; \bar{\mathbf{n}})$.

Figure 10 shows the χ^2 values obtained as an increasing number of PCs is included, following Equation (3.5), for the same least, intermediate, and most extreme cases considered in Figure 9. The PCA-based approach implemented in **CoCoA**, parameterize the photo-z uncertainty through $\bar{\mathbf{n}}(z) + \sum_i u_i \mathbf{U}_i(z)$, and evaluates χ^2 using the full likelihood expression given in Equation (4.6). That said, the work of [1], which forms the basis of our analysis, provides a linearized approximation for χ^2 , given in their Equation 17. We therefore compare the χ^2 evaluated using the full likelihood implemented in **CoCoA**, with the corresponding linearized expression of [1]. We highlight, however, that the comparison of these two cases we do in the following are not meant to indicate which one is “better”, but to provides a consistency check between our numerical implementation in **CoCoA** (as part of the Roman HLIS Cosmology PIT analysis pipeline) with the the analytical linearized approximation of the precursor work [1].

Figure 10 shows that the linearized approximation to χ^2 decays more rapidly than the full χ^2 evaluations. This behavior is expected: the linearized case depends only on the sum of the eigenvalues from the eigensystem decomposition optimized via the Fisher matrix in Equation (3.6) (see [1] for further details). In contrast, the weighted and unweighted full χ^2 evaluations exhibit a nontrivial dependence on the PC modes of Equation (3.5) through the full likelihood expression in Equation (4.6), as computed with **CoCoA**. Nevertheless, the full χ^2 evaluation for the weighted PCA case exhibits a decay similar to that of the linearized approximation, demonstrating the consistency of our numerical implementation in **CoCoA**. By contrast, the weighted case outperforms the unweighted one, as expected, since the Fisher matrix weights the PC modes by emphasizing directions in parameter space that are better constrained, thereby improving the stability and accuracy of the reconstructed observables. Although this behavior may seem obvious, we include the unweighted χ^2 evaluation to underscore the critical role of the Fisher matrix in optimizing the χ^2 computation.

Although $\chi_{\text{ini},\text{least}}^2 \ll \chi_{\text{ini},\text{most}}^2$, we can see from Figure 10 that this does not guarantee faster convergence of the “least extreme” case compared to the “most extreme” one. The threshold of $\chi^2 \leq 0.1$ is achieved nearly at 20 PCs for each extreme scenario. This result suggests that χ_{ini}^2 serves only to set a higher bias, not to guarantee a faster drop in χ^2 when more PCs are included. This makes sense: any \mathbf{n} shares the same space spanned by the PC modes, which are ordered by the amount of variance they explain in the realizations, from highest to lowest. If a given $\mathbf{n}(z)$ is the “least extreme”, $\mathcal{O}(\chi_i^2) \leq 1$, then we have to add higher order PCs to see significant drop in the χ^2 . If $\mathbf{n}(z)$ is the “most extreme” scenario, $\mathcal{O}(\chi_i^2) \geq 10^3$, then just adding the first PCs causes a faster drop in χ^2 . Once the most relevant modes are included, χ^2 starts converging slowly towards zero because the highest modes do not add significant information. In Figure 10, from 0-10 PCs, the “least extreme” drops from $\chi_i^2 = 5$, to $\chi^2 = 1.6$, while the “most extreme” drops three orders of magnitudes, from $\chi_i^2 = 1004$ to $\chi^2 = 2.5$.

We note, however, that we are comparing only three realizations within a landscape of one million. Moreover, because the full likelihood in Equation (4.6) is a nonlinear function of the redshift distribution computed numerically with **CoCoA**, we refrain from generalizing the decay of the full χ^2 evaluations as a function of the number of PC modes; in fact, χ^2 can

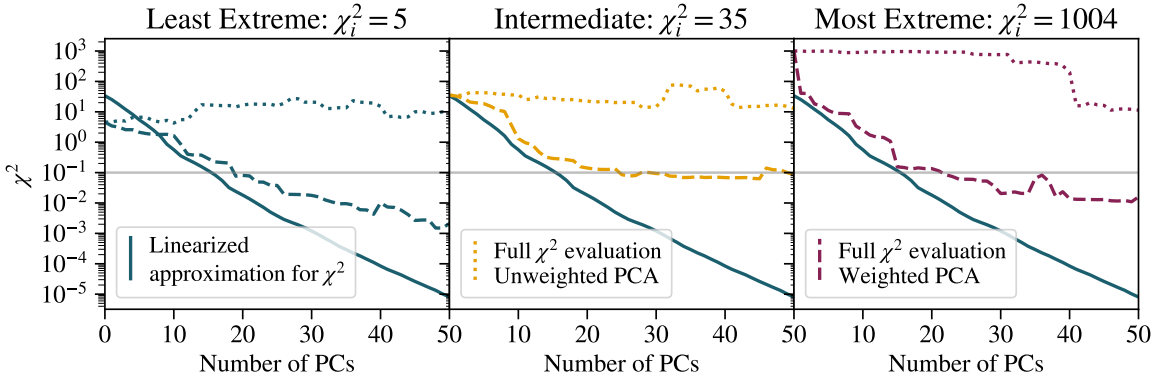


Figure 10. The χ^2 as a function of the number of PCs. The solid line shows the linearized approximation, while the dotted and dashed lines show the full χ^2 evaluations using the unweighted and weighted PCA, respectively. The titles “least extreme” ($\chi_i^2 = 5$), “intermediate” ($\chi_i^2 = 35$), and “most extreme” ($\chi_i^2 = 1004$) refer to the value of χ^2 at zero PCs. The gray horizontal line marks $\chi^2 = 0.1$ and indicates the number of PCs required to remain below this threshold: approximately 20 PCs for the least and most extreme realizations and about 25 PCs for the intermediate case. Beyond ~ 20 PCs, adding more modes does not yield a significant gain in information, as discussed further in Fig. 11.

occasionally rise before decreasing again. Although many factors can affect the overall trend—such as the simulated redshift distributions, the construction of the fiducial cosmic shear data vector, the scale cuts, and the data covariance matrix—it is notable that the weighted PCA in the full χ^2 evaluations tends to approach the linearized approximation discussed by [1], underscoring the consistency of our implementation in CoCoA.

5.2 Comparison between PCA and mean-shift uncertainty parameterizations

We use the least, intermediate, and most extreme cases from Figure 10 to run Markov Chain Monte Carlo, assessing the bias-mitigation performance of the weighted PCA approach versus the standard mean-shift method. Figure 12 presents the 1D constraints on Ω_m and S_8 with 2σ error bars. The left column shows how these constraints vary with the number of PCs. For the least extreme and intermediate scenarios, including additional PCs does not improve the constraints on Ω_m and S_8 . This is expected, as the initial χ_{ini}^2 values—corresponding to no mitigation (# of PCs = 0)—are already low: 5 and 35, respectively. The same conclusion applies to the mean-shift approach (right column). Notice, however, that widening the prior on Δ_z^i by nearly a factor of 3.33 (from $\text{Gauss}(0, 0.003)$ to $\text{Gauss}(0, 0.01)$) improves the accuracy, but warrants an increase in the error bars of Ω_m and S_8 .

The most stringent test for the PCA and mean-shift schemes for mitigating photo-z systematics occurs in the most extreme scenario. We observe by Figure 12 a clear improvement in the bias mitigation of Ω_m as additional PCs are included. With just one PC, Ω_m falls within 2σ of the fiducial value of 0.3, whereas the mean-shift approach does not reach the same level of agreement for the tightest prior, but does if the Gaussian width is increased to 0.01 as indicated by the hollow square in Figure 12.

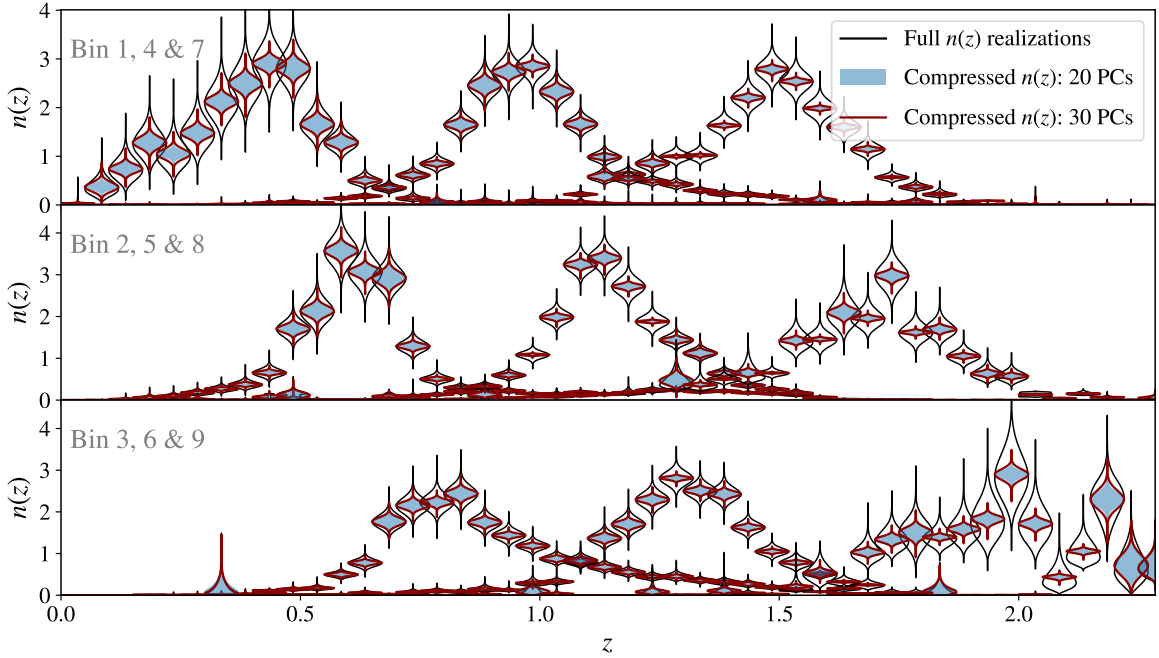


Figure 11. Violin plots of the redshift distribution $n(z)$ for 9 tomographic bins and 46 redshift sub-bins. The black contours show the full set of 10^6 $n(z)$ realizations for the Roman W1–D1 scenario. The blue and dark-red contours correspond to compressed representations using 20 and 30 principal components, respectively. The 30-mode case does not provide additional information compared to the 20-mode case, indicating that 20 principal components are sufficient.

5.3 The impact of Roman deep field design on $n(z)$ estimation

The results presented so far consider the situation where the PC modes were trained on the same Roman observing scenario (i.e., W1–D1) that was used to generate the fiducial synthetic data vector. In this section, we explore training and testing with different Roman observing scenarios (see Table 1; e.g., using W1–D2 for training and W1–D1 for testing). The aim of this exploration is to check the robustness of the weighted PCA model for describing data outside of the sample used to train the PCs. In the real analysis, the PC modes may be trained on simulations, but the data vector will be measured from observations. As shown in

PC training (PCs)	W1-D234	W2-D234	W3-D24
Fiducial ξ_{\pm} data vector (DV)	W1-D1	W2-D1	W3-D1

Table 3. Combinations of Roman observing scenarios for the simulated analyses.

the lower-triangle panel of Figure 7, using PCs and synthetic ξ_{\pm} data vectors derived from different Roman scenarios (the mixing case) introduces a slight skewness in the distribution of the PC amplitudes, though we still adopt a Gaussian (0, 1) prior in the MCMC runs. As in the non-mixing case, we must choose a redshift distribution to construct the fiducial synthetic ξ_{\pm} data vector: for the non-mixing analysis we use the Least Extreme, Intermediate, and Most Extreme cases, while for the mixing case we use the mean of the one million redshift distributions. Table 3 summarizes the analysis choices for the mixed-scenario setup. In this

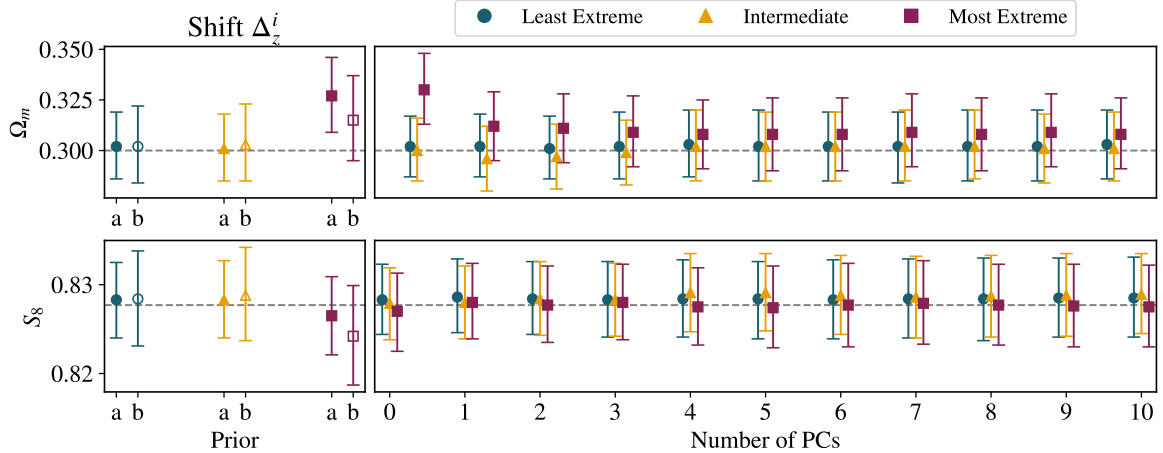


Figure 12. Constraints on Ω_m and S_8 at 2σ for the mean-shift and PCA methods for photo- z systematic parameterization. The former considers nine parameters Δ_z^i , corresponding to the number of tomographic bins, and is analyzed under two priors, “a” and “b” (see Table 2). The PCA approach is analyzed under the same three extreme scenarios as in Figure 10, i.e., synthetic cosmic shear data vectors generated with a specific $n(z)$ such that, when computing the chi-squared at zero PCs, they yield one of three cases: $\chi_i^2 = 5$ (“least extreme”), $\chi_i^2 = 35$ (“intermediate”), and $\chi_i^2 = 1004$ (“most extreme”).

configuration, the PCs are computed from the Roman deep-field scenarios D2, D3, and D4 (i.e., with magnitude errors, and see Table 1), while the ξ_{\pm} data vector is generated from the idealized deep-field W123-D1, i.e., error free scenarios.

In Figure 13, we show the 2σ constraints on Ω_m and S_8 for both the PCA and mean-shift mitigation schemes. For the combinations (DV: W1-D1, PCs: W1-D234), (DV: W2-D1, PCs: W2-D234), and (DV: W3-D1, PCs: W3-D24), the two methods remain consistent with each other and yield comparable constraints for most part of these combinations. However, both approaches are challenged in addressing the bias in two specific situations; The first case is indicated by the orange circles that considers the combination (DV: W1-D1, PCs: W1-D3). The PCA method mitigate the bias in S_8 once three or more PC modes are added. The mean-shift approach does not recover the fiducial S_8 value at 2σ for the tighter prior “a”, unless the broader one “b” is assumed.

The second case is illustrated by the light-green squares, corresponding to the combination (DV: W2-D1, PCs: W2-D3), which exhibits a strong bias. The mean-shift approach fails to mitigate the bias in Ω_m under the more restrictive prior “a”, except when the broader prior “b” is adopted, which warrants an increased error bars. Conversely, PCs constructed from W2-D3—even when including up to five modes—do not meaningfully improve constraints on the higher-order moments of the redshift distribution for the W2-D1 scenario. The deep tiers (D2-D4) fields with artificially inserted magnitude errors, will cause biases when recovering cosmological constraints. Only D1 is error free. This trend could imply that an artificially inserted error in the larger field (lower cosmic variance) shows up as a stronger bias in cosmology rather compared to the same error inserted in the smaller field (larger cosmic variance).

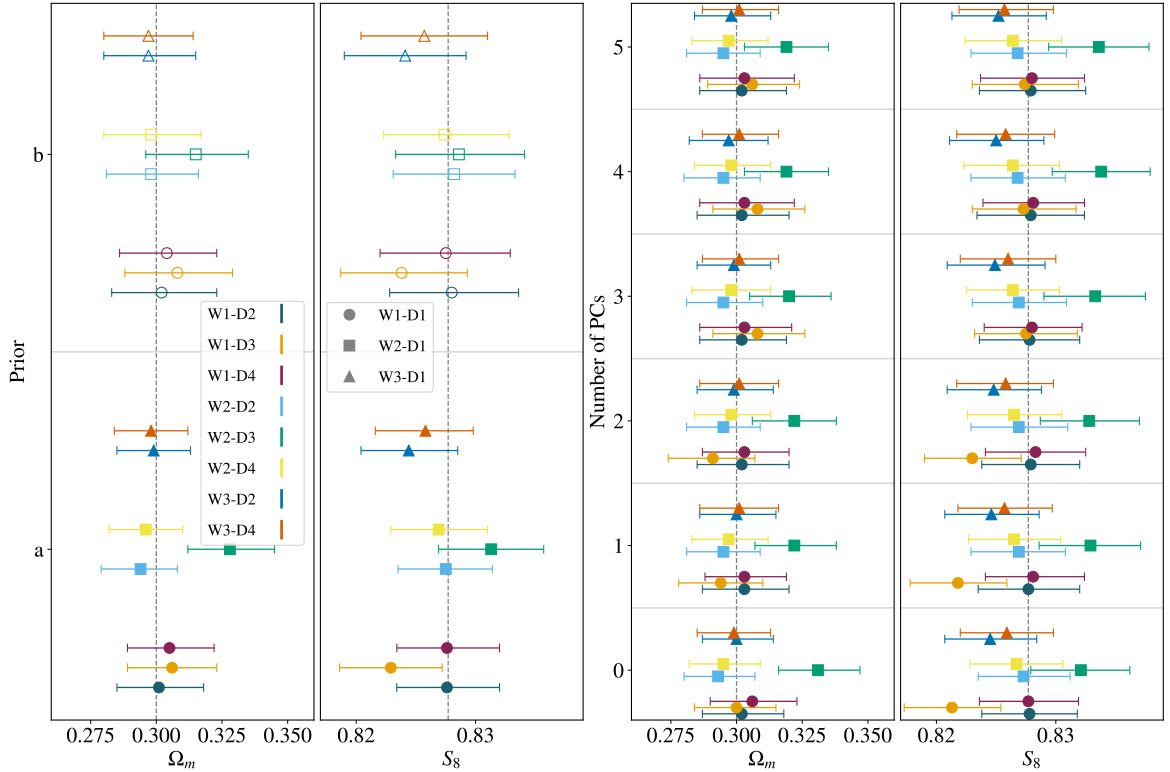


Figure 13. Constraints on Ω_m and S_8 at the 2σ confidence level. From left to right; the first two columns are constraints using the mean-shift approach for a tight prior (“a”) and wide prior (“b”). The last two columns, use the PCA method up to five PCs. The markers (DV: circles, squares, and triangles) indicate the Roman scenario used to generate the synthetic ξ_{\pm} data vector from a particular mean redshift distribution; circles correspond to $\bar{n}(z)$ from W1-D1, squares from W2-D1, and triangles from W3-D1. For the PCA method, the different colors denote the Roman scenarios employed to construct the PCs.

6 Conclusion

Designing a balance of imaging at different depths is critical for the goals of the HLWAS; probe the growth of the large scale structure and the expansion of the Universe with weak gravitational lensing and galaxy clustering, as well enabling several of others general astrophysics science. The nominal (in-guide) HLWAS consider a deep tier of 19.2 deg^2 providing crucial calibration data and a wide tier of 2700 deg^2 in H-band only (see [58] for further details). Specifically, the tomographic analysis of weak gravitational lensing is a powerful probe of the late Universe; however, uncertainties in the redshift distribution can bias the cosmological analysis and ultimately impede our ability to distinguish between dark energy models. In this work, we explore two ways of modeling redshift-distribution uncertainties for the Roman Space Telescope: the standard mean-shift parameterization and the newer PCA-based approach proposed in [1], which was adopted in the DES Y6 analyses by [32] and [33]. We implemented the PCA-based approach of [1] in the CoCoA code, which is part of the Roman HLIS Cosmology PIT analysis pipeline. To test our PCA-based implementation in CoCoA for modeling uncertainties in the redshift distribution and to assess its impact on cos-

ological parameter inference, we used the **Cardinal** to generate a mock galaxy catalogs and the SOMPZ methodology for bin assignment and draw millions of redshift-distributions. The uncertainty of the redshift distributions are to some extent stemmed from the assumptions of the wide- and deep-tiers configurations, such as the magnitude error, exposure times, filters, area and limiting magnitude in the H band. As a result, the choice of wide- and deep-tier configurations affects the uncertainty in the estimated redshift distributions and propagates into biases in the inferred cosmological parameters.

In this work, we therefore explore a wide range of scenarios: three wide tiers, labeled W1, W2, and W3, and four deep tiers, labeled D1, D2, D3, and D4. We combine these tiers to form a set of eleven possible Roman HLWAS survey scenarios: W1-D1, W1-D2, W1-D3, W1-D4, W2-D1, W2-D2, W2-D3, W2-D4, W3-D1, W3-D2, and W3-D4. We do not include the W3-D3 configuration, as it does not probe an additional calibration regime beyond those already explored and is therefore outside the scope of our targeted stress test of enlarged deep-field areas for the baseline wide tiers (W1 and W2). In comparison with the nominal HLWAS recommended by the ROTAC, i.e., a deep tier covering 19.2 deg^2 and a wide tier covering 2700 deg^2 , the deep tiers D1, D2, and D4 cover the same area of 20 deg^2 , while the deep tier D3 covers 40 deg^2 . Therefore, wide tiers paired with D3 deviate from the ROTAC recommendations. However, we include these non-recommended scenarios to stress test our PCA implementation in the **CoCoA** code, as it is an essential component of the HLIS PIT pipeline. We then perform multiple MCMC analyses using both mitigation schemes—the mean-shift and PCA approaches—and compare their bias mitigation and constraining power on the cosmological parameters Ω_m and S_8 .

We found that when the ξ_{\pm} data vector (generated from an $\mathbf{n}(z)$ realization) is not strongly miscalibrated—i.e., has a low initial value of $\chi_{\text{ini}}^2 \sim O(10)$ —relative to our best estimate of the redshift distribution (the mean $\bar{\mathbf{n}}(z)$ across realizations), both the mean-shift and PCA-based methods provide comparable constraints on the parameters Ω_m and S_8 , a trend consistent with the findings of [32] in the DES Y6 cosmic-shear analysis. However, meaningful differences between the two approaches emerge when we introduce moderate ($\chi_{\text{ini}}^2 \sim O(100)$) to strong ($\chi_{\text{ini}}^2 \sim O(1000)$) miscalibrations. In these regimes, using a tight Gaussian prior (mean = 0, std = 0.003) on the Δ_z^i parameters fails to mitigate the resulting biases in Ω_m and S_8 . Relaxing the prior to a wider Gaussian (mean = 0, std = 0.01) helps reduce these biases, but at the cost of mildly larger error bars. In the most extreme scenario, for the PCA-based approach (see Figure 12), using 5 PCs mitigates the bias in Ω_m , and adding additional PCs does not significantly improve the constraints, whereas the 9 Δ_z^i parameters yields slightly weaker constraints under the wider prior. It is also worth noting that we use a much wider Gaussian prior (mean = 0, std = 1) on the PC amplitudes, u_i , compared with the mean-shift approach (std = 0.003 and 0.01), and even under these conditions, the PCA-based method provides meaningful constraints on the cosmological parameters. With a more informative prior on these amplitudes, we would expect even tighter bounds on Ω_m and S_8 . Although the PCA-based approach analyzed here performs comparably to the standard mean-shift parameterization in mitigating biases, we emphasize that these results are obtained under deliberately extreme scenarios, selected primarily to stress-test the $n(z)$ PCA implementation in **CoCoA**. When averaged over realizations, the PCA and mean-shift approaches yield consistent cosmological constraints. Nonetheless, our results indicate that the PCA-based method provides a flexible and potentially promising framework for modeling redshift-distribution uncertainties and may offer modest improvements in constraining power in certain regimes.

In summary, it is worthy of attention that every scenario with wide- and deep-tier close to the nominal HLWAS, i.e., D1, D2 and D4, possess constraints on Ω_m and S_8 within 2σ confidence level of its respective fiducial values via PCA-based approach or the standard mean-shift method. However, the scenarios with deep tier D3 are the most challenging in mitigating biases on these same cosmological parameters; for the scenario W1-D3, the bias on S_8 is mitigated with three PC modes, but one needs to relax the prior condition with the mean-shift approach in order to attain the mitigate the bias. On the other hand, the scenario W2-D3 is the most challenge, indeed the PCA-method could not mitigate the bias for none of the parameters, Ω_m neither S_8 , and the mean shift only mitigate the bias on Ω_m with the relaxed prior, that implies slightly increased error bars (check Figure 13 for further details). Essentially, the difficulty in mitigate bias on Ω_m and S_8 with the PC modes derived from W2-D3 is due to the low variability in the W2-D3 realizations due to the larger deep-field area (40 deg^2), which reduces cosmic variance and limits the informativeness of the PCs. The results presented here demonstrates that the PCA-based approach for modeling uncertainties in redshift distribution performs well in most cases, and a part of the instances where its effectiveness is limited, as we highlighted above, the PCA-based framework showed up as viable and possible modeling of photo-z uncertainties to be exported to others imaging surveys such as LSST and Euclid.

Future analyses using the PCA-based technique could incorporate new simulated Roman redshift distributions from **Cardinal** and the SOMPZ methodology, explore models beyond ΛCDM -such as dynamical dark energy models (e.g., $w_0w_a\text{CDM}$)-extend the analysis to the 3×2 correlation functions, and employ emulators to reduce computational costs when deriving cosmological parameter constraints.

Acknowledgments

DHFS is supported by the Jet Propulsion Laboratory and the California Institute of Technology. This research was carried out at the Jet Propulsion Laboratory, California Institute of Technology, and was sponsored by the National Aeronautics and Space Administration (80NM0018D0004). This work was supported by the NASA ROSES grant 22-ROMAN11-0011, contract number 80NM0024F0012, via a JPL subaward. The High Performance Computing resources used in this investigation were provided by funding from the JPL Enterprise Technology, Strategy, and Cybersecurity Directorate. We thank Gary M. Bernstein for insightful discussions.

References

- [1] G. Bernstein, W. Assigies Doumèrg, M.A. Troxel, A. Alarcon, A. Amon, G. Giannini et al., *Sampling Bayesian probabilities given only sampled priors*, *arXiv e-prints* (2025) arXiv:2506.00758 [2506.00758].
- [2] R. Mandelbaum, *Weak lensing for precision cosmology*, *Ann. Rev. Astron. Astrophys.* **56** (2018) 393 [1710.03235].
- [3] D.H. Weinberg, M.J. Mortonson, D.J. Eisenstein, C. Hirata, A.G. Riess and E. Rozo, *Observational probes of cosmic acceleration*, *physrep* **530** (2013) 87 [1201.2434].
- [4] G.M. Bernstein, *Comprehensive Two-Point Analyses of Weak Gravitational Lensing Surveys*, *Astrophys. J.* **695** (2009) 652 [0808.3400].
- [5] M. Bartelmann and P. Schneider, *Weak gravitational lensing*, *Phys. Rept.* **340** (2001) 291 [astro-ph/9912508].
- [6] P. Catelan, M. Kamionkowski and R.D. Blandford, *Intrinsic and extrinsic galaxy alignment*, *mnras* **320** (2001) L7 [astro-ph/0005470].
- [7] C.M. Hirata, R. Mandelbaum, M. Ishak, U. Seljak, R. Nichol, K.A. Pimbblet et al., *Intrinsic galaxy alignments from the 2SLAQ and SDSS surveys: Luminosity and redshift scalings and implications for weak lensing surveys*, *Mon. Not. Roy. Astron. Soc.* **381** (2007) 1197 [astro-ph/0701671].
- [8] R. Mandelbaum, C. Blake, S. Bridle, F.B. Abdalla, S. Brough, M. Colless et al., *The WiggleZ Dark Energy Survey: direct constraints on blue galaxy intrinsic alignments at intermediate redshifts*, *mnras* **410** (2011) 844 [0911.5347].
- [9] G.M. Bernstein and M. Jarvis, *Shapes and Shears, Stars and Smears: Optimal Measurements for Weak Lensing*, *aj* **123** (2002) 583 [astro-ph/0107431].
- [10] T. Eifler, E. Krause, S. Dodelson, A. Zentner, A. Hearin and N. Gnedin, *Accounting for Baryonic Effects in Cosmic Shear Tomography: Determining a Minimal Set of Nuisance Parameters Using PCA*, *Mon. Not. Roy. Astron. Soc.* **454** (2015) 2451 [1405.7423].
- [11] H.-J. Huang, T. Eifler, R. Mandelbaum and S. Dodelson, *Modelling baryonic physics in future weak lensing surveys*, *Mon. Not. Roy. Astron. Soc.* **488** (2019) 1652 [1809.01146].
- [12] G. Bernstein and D. Huterer, *Catastrophic photometric redshift errors: weak-lensing survey requirements*, *mnras* **401** (2010) 1399 [0902.2782].
- [13] W. Hu, *Power spectrum tomography with weak lensing*, *Astrophys. J. Lett.* **522** (1999) L21 [astro-ph/9904153].
- [14] Z. Ma, W. Hu and D. Huterer, *Effects of Photometric Redshift Uncertainties on Weak-Lensing Tomography*, *apj* **636** (2006) 21 [astro-ph/0506614].
- [15] DES collaboration, *Dark Energy Survey Year 1 Results: Redshift distributions of the weak lensing source galaxies*, *Mon. Not. Roy. Astron. Soc.* **478** (2018) 592 [1708.01532].
- [16] DES collaboration, *Dark Energy Survey Year 1 Results: Cross-Correlation Redshifts – Methods and Systematics Characterization*, *Mon. Not. Roy. Astron. Soc.* **477** (2018) 1664 [1709.00992].
- [17] DES collaboration, *Dark Energy Survey Year 1 Results: Cross-Correlation Redshifts in the DES – Calibration of the Weak Lensing Source Redshift Distributions*, *arXiv e-prints* (2017) [1710.02517].
- [18] N. Benitez, *Bayesian photometric redshift estimation*, *Astrophys. J.* **536** (2000) 571 [astro-ph/9811189].
- [19] DES collaboration, *Dark Energy Survey Year 1 results: Cosmological constraints from cosmic shear*, *Phys. Rev. D* **98** (2018) 043528 [1708.01538].

[20] C. Laigle et al., *The COSMOS2015 Catalog: Exploring the $1 < z < 6$ Universe with half a million galaxies*, *Astrophys. J. Suppl.* **224** (2016) 24 [[1604.02350](#)].

[21] DES collaboration, *Dark Energy Survey year 1 results: Cosmological constraints from galaxy clustering and weak lensing*, *Phys. Rev. D* **98** (2018) 043526 [[1708.01530](#)].

[22] DES collaboration, *Dark Energy Survey Year 3 Results: Photometric Data Set for Cosmology*, *Astrophys. J. Suppl.* **254** (2021) 24 [[2011.03407](#)].

[23] DES collaboration, *Dark energy survey year 3 results: weak lensing shape catalogue*, *Mon. Not. Roy. Astron. Soc.* **504** (2021) 4312 [[2011.03408](#)].

[24] DES collaboration, *Phenotypic redshifts with self-organizing maps: A novel method to characterize redshift distributions of source galaxies for weak lensing*, *Mon. Not. Roy. Astron. Soc.* **489** (2019) 820 [[1901.05005](#)].

[25] DES, EBOSS collaboration, *Dark Energy Survey Year 3 Results: clustering redshifts – calibration of the weak lensing source redshift distributions with redMaGiC and BOSS/eBOSS*, *Mon. Not. Roy. Astron. Soc.* **510** (2022) 1223 [[2012.08569](#)].

[26] DES collaboration, *Dark Energy Survey Year 3 results: Exploiting small-scale information with lensing shear ratios*, *Phys. Rev. D* **105** (2022) 083529 [[2105.13542](#)].

[27] DES collaboration, *Dark Energy Survey Year 3 results: redshift calibration of the weak lensing source galaxies*, *Mon. Not. Roy. Astron. Soc.* **505** (2021) 4249 [[2012.08566](#)].

[28] DES collaboration, *Dark Energy Survey Year 3 results: Cosmology from cosmic shear and robustness to modeling uncertainty*, *Phys. Rev. D* **105** (2022) 023515 [[2105.13544](#)].

[29] DES collaboration, *Dark Energy Survey Year 3 results: Cosmology from cosmic shear and robustness to data calibration*, *Phys. Rev. D* **105** (2022) 023514 [[2105.13543](#)].

[30] DES collaboration, *Dark Energy Survey Year 3 results: Cosmological constraints from galaxy clustering and weak lensing*, *Phys. Rev. D* **105** (2022) 023520 [[2105.13549](#)].

[31] DES collaboration, *Dark Energy Survey Year 3 results: marginalization over redshift distribution uncertainties using ranking of discrete realizations*, *Mon. Not. Roy. Astron. Soc.* **511** (2022) 2170 [[2109.09636](#)].

[32] B. Yin, A. Amon, A. Campos, M.A. Troxel, W. d'Assignies, G.M. Bernstein et al., *Dark Energy Survey Year 6 Results: Redshift Calibration of the Weak Lensing Source Galaxies*, *arXiv e-prints* (2025) arXiv:2510.23566 [[2510.23566](#)].

[33] G. Giannini, A. Alarcon, W. d'Assignies, G.M. Bernstein, M.A. Troxel, C. Chang et al., *Dark Energy Survey Year 6 Results: Redshift Calibration of the MagLim++ Lens Sample*, *arXiv e-prints* (2025) arXiv:2509.07964 [[2509.07964](#)].

[34] O. Doré et al., *WFIRST: The Essential Cosmology Space Observatory for the Coming Decade*, *baas* (2019) [[1904.01174](#)].

[35] WFIRST collaboration, *WFIRST Science Investigation Team "Cosmology with the High Latitude Survey" Annual Report 2017*, *arXiv e-prints* (2018) [[1804.03628](#)].

[36] R. Akeson, L. Armus, E. Bachelet, V. Bailey, L. Bartusek, A. Bellini et al., *The wide field infrared survey telescope: 100 hubbles for the 2020s*, *arXiv preprint arXiv:1902.05569* (2019) .

[37] T. Eifler et al., *Cosmology with the Roman Space Telescope – multiprobe strategies*, *Mon. Not. Roy. Astron. Soc.* **507** (2021) 1746 [[2004.05271](#)].

[38] R. Hounsell et al., *Simulations of the WFIRST Supernova Survey and Forecasts of Cosmological Constraints*, *Astrophys. J.* **867** (2018) 23 [[1702.01747](#)].

[39] L. Wenzl, C. Doux, C. Heinrich, R. Bean, B. Jain, O. Doré et al., *Cosmology with the Roman Space Telescope – Synergies with CMB lensing*, *Mon. Not. Roy. Astron. Soc.* **512** (2022) 5311 [[2112.07681](#)].

[40] LSST collaboration, *LSST: from Science Drivers to Reference Design and Anticipated Data Products*, *Astrophys. J.* **873** (2019) 111 [[0805.2366](#)].

[41] EUCLID collaboration, *Euclid. I. Overview of the Euclid mission*, *Astron. Astrophys.* **697** (2025) A1 [[2405.13491](#)].

[42] C.-H. To, J. DeRose, R.H. Wechsler, E. Rykoff, H.-Y. Wu, S. Adhikari et al., *Buzzard to Cardinal: Improved Mock Catalogs for Large Galaxy Surveys*, *Astrophys. J.* **961** (2024) 59 [[2303.12104](#)].

[43] R.H. Wechsler and J.L. Tinker, *The Connection Between Galaxies and Their Dark Matter Halos*, *araa* **56** (2018) 435 [[1804.03097](#)].

[44] J. DeRose, M.R. Becker and R.H. Wechsler, *Modeling Redshift-space Clustering with Abundance Matching*, *Astrophys. J.* **940** (2022) 13 [[2105.12104](#)].

[45] A.V. Kravtsov, A.A. Berlind, R.H. Wechsler, A.A. Klypin, S. Gottlöber, B. Allgood et al., *The Dark Side of the Halo Occupation Distribution*, *apj* **609** (2004) 35 [[astro-ph/0308519](#)].

[46] C. Conroy, R.H. Wechsler and A.V. Kravtsov, *Modeling Luminosity-dependent Galaxy Clustering through Cosmic Time*, *apj* **647** (2006) 201 [[astro-ph/0512234](#)].

[47] B.V. Lehmann, Y.-Y. Mao, M.R. Becker, S.W. Skillman and R.H. Wechsler, *The Concentration Dependence of the Galaxy-Halo Connection: Modeling Assembly Bias with Abundance Matching*, *Astrophys. J.* **834** (2017) 37 [[1510.05651](#)].

[48] J. DeRose, R.H. Wechsler, M.R. Becker, M.T. Busha, E.S. Rykoff, N. MacCrann et al., *The Buzzard Flock: Dark Energy Survey Synthetic Sky Catalogs*, *arXiv e-prints* (2019) [arXiv:1901.02401](#) [[1901.02401](#)].

[49] DES collaboration, *Dark Energy Survey Year 3 results: Cosmology from combined galaxy clustering and lensing validation on cosmological simulations*, *Phys. Rev. D* **105** (2022) 123520 [[2105.13547](#)].

[50] E. Rozo, E.S. Rykoff, A. Abate, C. Bennett, M. Crocce, C. Davis et al., *redMaGiC: selecting luminous red galaxies from the DES Science Verification data*, *mnras* **461** (2016) 1431 [[1507.05460](#)].

[51] E.S. Rykoff, E. Rozo, D. Hollowood, A. Bermeo-Hernandez, T. Jeltema, J. Mayers et al., *The RedMaPPer Galaxy Cluster Catalog From DES Science Verification Data*, *apjs* **224** (2016) 1 [[1601.00621](#)].

[52] R.H. Wechsler, J. DeRose, M.T. Busha, M.R. Becker, E. Rykoff and A. Evrard, *ADDGALS: Simulated Sky Catalogs for Wide Field Galaxy Surveys*, *apj* **931** (2022) 145 [[2105.12105](#)].

[53] M.R. Blanton, J. Brinkmann, I. Csabai, M. Doi, D. Eisenstein, M. Fukugita et al., *Estimating Fixed-Frame Galaxy Magnitudes in the Sloan Digital Sky Survey*, *aj* **125** (2003) 2348 [[astro-ph/0205243](#)].

[54] A.L. Coil, M.R. Blanton, S.M. Burles, R.J. Cool, D.J. Eisenstein, J. Moustakas et al., *The PRISM Multi-object Survey (PRIMUS). I. Survey Overview and Characteristics*, *apj* **741** (2011) 8 [[1011.4307](#)].

[55] A. Campos, B. Yin, S. Dodelson, A. Amon, A. Alarcon, C. Sánchez et al., *Enhancing weak lensing redshift distribution characterization by optimizing the Dark Energy Survey Self-Organizing Map Photo-z method*, *arXiv e-prints* (2024) [arXiv:2408.00922](#) [[2408.00922](#)].

[56] C. Sánchez, M. Raveri, A. Alarcon and G.M. Bernstein, *Propagating sample variance uncertainties in redshift calibration: simulations, theory and application to the COSMOS2015 data*, *Mon. Not. Roy. Astron. Soc.* **498** (2020) 2984 [[2004.09542](#)].

[57] A. Lewis and A. Challinor, “CAMB: Code for Anisotropies in the Microwave Background.” Astrophysics Source Code Library, record ascl:1102.026, Feb., 2011.

[58] R. Observations Time Allocation Committee and C. Community Survey Definition Committees, *Roman Observations Time Allocation Committee: Final Report and Recommendations*, *arXiv e-prints* (2025) arXiv:2505.10574 [2505.10574].

[59] M.R. Becker, *CALCLEN: Weak lensing simulations for large-area sky surveys and second-order effects in cosmic shear power spectra*, Ph.D. thesis, University of Chicago, Jan., 2013.

[60] E. Krause and T. Eifler, *cosmolike - cosmological likelihood analyses for photometric galaxy surveys*, *mnras* **470** (2017) 2100 [1601.05779].

[61] X. Fang, T. Eifler and E. Krause, *2D-FFTLog: Efficient computation of real space covariance matrices for galaxy clustering and weak lensing*, *Mon. Not. Roy. Astron. Soc.* **497** (2020) 2699 [2004.04833].

[62] J. Torrado and A. Lewis, *Cobaya: Code for Bayesian Analysis of hierarchical physical models*, *JCAP* **05** (2021) 057 [2005.05290].

[63] A. Lewis, A. Challinor and A. Lasenby, *Efficient computation of CMB anisotropies in closed FRW models*, *apj* **538** (2000) 473 [astro-ph/9911177].

[64] A. Lewis, *GetDist: a Python package for analysing Monte Carlo samples*, *JCAP* **08** (2025) 025 [1910.13970].

[65] A. Stebbins, *Weak Lensing On the Celestial Sphere*, *arXiv e-prints* (1996) astro [astro-ph/9609149].

[66] E. Krause, X. Fang, S. Pandey, L.F. Secco, O. Alves, H. Huang et al., *Dark Energy Survey Year 3 Results: Multi-Probe Modeling Strategy and Validation*, *arXiv e-prints* (2021) arXiv:2105.13548 [2105.13548].

[67] D.N. Limber, *The Analysis of Counts of the Extragalactic Nebulae in Terms of a Fluctuating Density Field.*, *apj* **117** (1953) 134.

[68] E. Krause, T.F. Eifler, J. Zuntz, O. Friedrich, M.A. Troxel, S. Dodelson et al., *Dark Energy Survey Year 1 Results: Multi-Probe Methodology and Simulated Likelihood Analyses*, *arXiv e-prints* (2017) arXiv:1706.09359 [1706.09359].

[69] DES collaboration, *Dark Energy Survey year 3 results: covariance modelling and its impact on parameter estimation and quality of fit*, *Mon. Not. Roy. Astron. Soc.* **508** (2021) 3125 [2012.08568].

[70] R. Takahashi, M. Sato, T. Nishimichi, A. Taruya and M. Oguri, *Revising the Halofit Model for the Nonlinear Matter Power Spectrum*, *Astrophys. J.* **761** (2012) 152 [1208.2701].

[71] P. Catelan, M. Kamionkowski and R.D. Blandford, *Intrinsic and extrinsic galaxy alignment*, *Mon. Not. Roy. Astron. Soc.* **320** (2001) L7 [astro-ph/0005470].

[72] C.M. Hirata and U. Seljak, *Intrinsic alignment-lensing interference as a contaminant of cosmic shear*, *Phys. Rev. D* **70** (2004) 063526 [astro-ph/0406275].

[73] S. Bridle and L. King, *Dark energy constraints from cosmic shear power spectra: impact of intrinsic alignments on photometric redshift requirements*, *New J. Phys.* **9** (2007) 444 [0705.0166].